



Cite this: *Phys. Chem. Chem. Phys.*,  
2025, 27, 844

Received 1st August 2024,  
Accepted 15th November 2024

DOI: 10.1039/d4cp03060e

rsc.li/pccp

# Sulfobetaine ionic liquid crystals based on strong acids: phase behavior and electrochemistry†

Alyna Lange,<sup>a</sup> Nadia Kapernaum,<sup>b</sup> Zaneta Wojnarowska,<sup>c</sup> Lea Holtzheimer,<sup>a</sup> Stefan Mies,<sup>a</sup> Vance Williams,<sup>d</sup> Frank Gießelmann<sup>b</sup> and Andreas Taubert<sup>a</sup>

A group of new zwitterion based ionic liquid crystals (ILCs) have been synthesized. Depending on the counter anion (mesylate or hydrogen sulfate) the phase behavior of the resulting ILCs is quite different. Mesylate based ILCs show complex phase behavior with multiple phases depending on the alkyl chain length. In contrast, hydrogen sulfate based systems always exhibit CoI<sub>1</sub> phases irrespective of the alkyl chain length. The latter show much larger ILC mesophase windows and are thermally stable up to ca. 200 °C. All ILCs show reasonable ionic conductivities of up to 10<sup>−4</sup> S cm<sup>−1</sup> at elevated temperatures, making these ILCs candidates for intermediate temperature ionic conductors.

## Introduction

Nafion, the fluorinated copolymer typically used as an electrolyte in polymer electrolyte membrane (PEM) fuel cells, only shows limited usability at temperatures above ca. 80 °C.<sup>1,2</sup> Therefore, especially for medium and high temperature fuel cells, the necessity to develop water-free electrolytes that maintain a high ionic conductivity at higher temperatures arises.<sup>2</sup> Ionic liquids (ILs) are promising materials to achieve high conductivities at intermediate temperatures between ca. 80 and 200 °C.<sup>2–4</sup> ILs often have low melting points, are not flammable and exhibit low vapour pressures making them attractive for electrolyte applications. Beside their wide electrochemical stability window they can also exhibit high thermal stabilities, which is again interesting for modern electrolytes.<sup>5,6</sup>

Most ILs only show low range order and their conductivities therefore show no anisotropy, meaning that the conductivity is identical in all directions. It may, however, be interesting to achieve anisotropic (ion) conduction in ILs, e.g. to improve ion transport in a specific direction in a fuel cell or battery. This can be achieved by mesoscale structuration of ILs, resulting in ionic liquid crystals (ILCs).<sup>7,8</sup> The nanosegregation needed to achieve liquid crystalline (LC) self-organisation of the

compounds is usually realized by introducing one or more long alkyl chains into the structure of the ILs.<sup>8–10</sup> By introducing this hydrophobic part, the immiscibility between the ionic head group and the long alkyl chains leads to the desired mesoscale phase separation of the ionic and the hydrophobic domains. This results in long range ordered structures, that is, LCs or (in the case of ILs) ILCs.<sup>8,10</sup>

Like ILs, ILCs are also composed of ions, bound to different extents by ionic interaction.<sup>8,11,12</sup> Thermotropic ILCs combine features of LCs and ILs (anisotropic conductivity, self-assembly and high ionic conductivities, electrochemical stability and “tuning” possibilities) and, like their non-ionic counterparts, they exhibit liquid crystalline phases between the solid and liquid states. Therefore, they are important candidates for flexible electronics or as safe and efficient electrolytes.<sup>8,11,13,14</sup>

For use as electrolytes in e.g. fuel cells, protic ILCs are needed.<sup>15</sup> These are commonly synthesized by an acid–base reaction between the respective long-chained acids and bases. By choice of the acid and base it is also possible to tune the physical properties of the resulting ILCs.<sup>8</sup> For satisfactory proton conduction, favorable transport of protons needs to be realized – and ILCs can facilitate this favorable transport due to their structure and anisotropic organization. The anisotropic mesoscale organization and concurrent separation of ionic and apolar domains in ILCs is therefore expected to enable fast target ion (proton) transport.<sup>8,16</sup> Indeed, Mukai *et al.* have shown that proton conduction in some ILCs is indeed higher in the LC (SmA) phase compared to the liquid phase and that these materials can be used for the development of 2D anisotropic ion conducting materials.<sup>8,17</sup>

To achieve effective transport and therefore high conduction of selected target ions, another feature can be introduced into the ILCs. Namely, the tethering of cationic and anionic sites into the same molecule, creating so-called zwitterions (ZIs).<sup>8,12</sup>

<sup>a</sup> Institute of Chemistry, University of Potsdam, Karl-Liebknecht-Straße 24-25, 14476 Potsdam-Golm, Germany. E-mail: alylange@uni-potsdam.de, andreas.taubert@uni-potsdam.de

<sup>b</sup> Institute of Physical Chemistry, University of Stuttgart, Pfaffenwaldring 55, Stuttgart, Germany

<sup>c</sup> Institute of Physics, University of Silesia in Katowice, 41-500 Chorzow, Poland

<sup>d</sup> Department of Chemistry, Simon Fraser University, 8888 University Drive, Burnaby, Canada

† Electronic supplementary information (ESI) available. See DOI: <https://doi.org/10.1039/d4cp03060e>



As described by Goossens *et al.*, in conventional ILs the transference number of target ions can be lowered significantly by the migration of other compound ions in the electric field.<sup>18</sup> As zwitterions exhibit net neutrality due to their positively and negatively charged moieties located in the same molecule, they are expected to not move in an applied (external) field.<sup>8</sup> This may lead to fast proton conduction *via* the Grotthuss mechanism rather than the slower vehicle mechanism because the movement of the larger ions (making up the IL or ILC) is essentially eliminated.<sup>18</sup> Phosphonium based zwitterionic protic LCs that exhibit lyotropic LC behavior and columnar phases for 1D proton conduction have already been shown by Ueda *et al.*<sup>19</sup> Moreover, Kobayashi *et al.* and Ichikawa *et al.* reported bicontinuous cubic ILCs on the basis of pyridinium ZIs for (solid) 3D proton conduction.<sup>15,20</sup>

The combination of a zwitterion with a Brønsted acid such as toluene sulfonic<sup>21–23</sup> or methanesulfonic<sup>23</sup> acid leads to zwitterionic ILs, where the proton is free to move between the sulfonate group of the zwitterion and the sulfonate group of the tosylate or mesylate anion, for example. Wojnarowska *et al.* have already shown that charge transport *via* the Grotthuss mechanism is promoted if methanesulfonate is used as the anion in a zwitterionic protic IL (PIL).<sup>24</sup> This article therefore describes the synthesis, the phase behavior, and the electrochemical properties of zwitterionic alkylammonium based protic ILCs with methanesulfonate and hydrogen sulfate anions *vs.* the influence of different alkyl chain lengths on the zwitterions and the type of anion (methanesulfonate or hydrogen sulfate). Fig. 1 shows the synthetic approach towards the ZI-based ILCs used in the current study.

## Experimental section

### Materials

*N,N*-Dimethyloctylamine (purity not specified by the supplier, Sigma-Aldrich), *N,N*-dimethyldecylamine (98%, Sigma-Aldrich), *N,N*-dimethyldodecylamine ( $\geq 90\%$ , TCI), *N,N*-dimethyltetradecylamine ( $\geq 95\%$ , Sigma-Aldrich), *N,N*-dimethylhexadecylamine ( $\geq 95\%$ , Sigma-Aldrich), 1-4-butanediol (99%, aber), sulfuric acid (98%, Roth), methanesulfonic acid (99%, Aldrich Chemical Co.), methanol (for synthesis, 99.5%, Roth), acetone (for synthesis, 99.5%, Roth), acetonitrile (99.9%, VWR),

ferrocene (97%, Alfa Aesar), and tetrabutylammonium hexafluorophosphate (98%, Merck) were employed in this study. All chemicals and materials were used as received.

## Preparation of zwitterions

All zwitterions were synthesized *via* an existing synthesis protocol.<sup>21–23</sup> Analytical data for these ZIs can be found in the ESI.†

Nomenclature of the ZIs is as follows:  $\text{DmC}_n\text{S}$ , where Dm is dimethyl,  $\text{C}_n$  is the alkyl tail with  $n$  = chain length of the alkyl tail ( $\text{C}_{10}$ – $\text{C}_{16}$ ), and S indicates the sulfonate group present in the zwitterion. For example,  $\text{DmC}_{10}\text{S}$  is the zwitterion (Fig. 1) with a  $\text{C}_{10}$  alkyl chain.

## Preparation of ionic liquid crystals

All ILCs were prepared using the same method. In a 100 mL round-bottom flask, the respective zwitterion was dissolved in a minimal amount of methanol *via* stirring with a magnetic stir bar. The scale was usually around 3 g of zwitterion and 5–10 mL of methanol. After complete dissolution of the zwitterion, an equimolar amount of the respective acid (sulfuric acid or methanesulfonic acid) was added *via* a syringe under ice-bath cooling. After the addition of the acids was finished, the mixture was allowed to warm up to room temperature. Subsequently, the solution was heated to 40 °C and stirred for 3–4 hours. Afterwards the solvent was removed by rotary evaporation and the resulting compound was dried under vacuum ( $10^{-2}$  mbar) for 24 hours. The appearance of the reaction products differed, as some were gels and some solid powders. Analytical data for all products can be found in the ESI.†

The nomenclature of the ILCs is as follows: the ZI is designated as described above. Mesylate based ILCs are labelled  $\text{DmC}_n\text{S MeSO}_3$  and hydrogen sulfate based ILCs are labelled  $\text{DmC}_n\text{S HSO}_4$ .

## Characterization and instrumentation

### Nuclear magnetic resonance spectroscopy

$^1\text{H}$ -NMR spectra were recorded on a Bruker Avance 400 MHz Spectrometer in  $\text{D}_2\text{O}$  at room temperature. For the longer

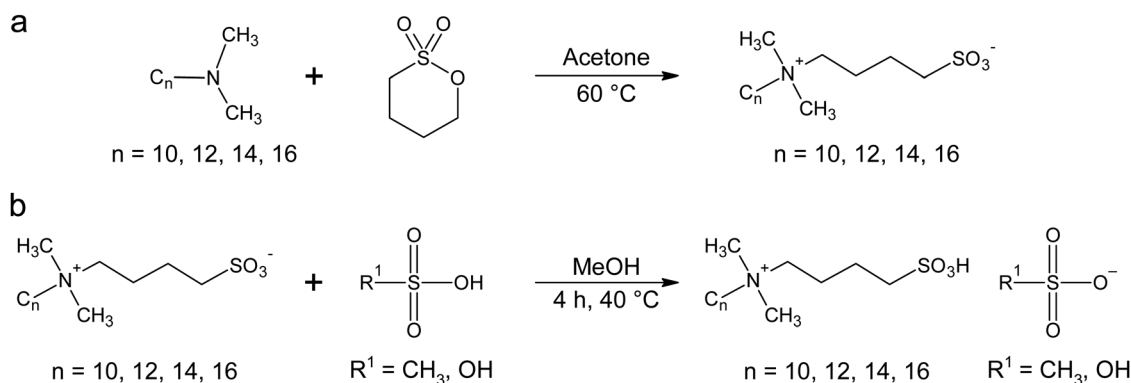


Fig. 1 Synthetic procedure for the zwitterionic ILCs: (a) synthesis of the sulfobetaine ZIs, and (b) synthesis of the zwitterionic ILCs.



chained compounds (C<sub>12</sub>–C<sub>16</sub>) small amounts of NaCl were added to the solution to improve solubility.

### Spectroscopy

Infrared (IR) spectra were recorded using the attenuated total reflection (ATR) mode on a Thermo Scientific NICOLET iS5 with ID7 ATR probe head. Spectra were taken from 500 to 4000 cm<sup>−1</sup> with a resolution of 2 cm<sup>−1</sup> and 64 scans per measurement.

### Thermal analysis

Simultaneous thermogravimetric analysis-differential thermal analysis (TGA-DTA) experiments were carried out using a Mettler Toledo TGA/DSC 3+ thermogravimetric analyzer from 30 to 600 °C with a heating rate of 10 K min<sup>−1</sup> under air in aluminium oxide crucibles with lids. The lids were used to avoid moisture uptake before the measurements, but also limit the measurement temperature to 600 °C.

Differential scanning calorimetry (DSC) measurements were carried out using a Netzsch Polyma DSC 214. DSC values were recorded from −100 to 200 °C using liquid nitrogen cooling and a heating rate of 10 K min<sup>−1</sup> or 5 K min<sup>−1</sup>. Heating and cooling cycles were repeated three times for reproducibility. Unless otherwise stated, data of the 2nd heating and cooling cycle are used and presented for analysis.

### Polarized optical microscopy (POM)

Optical microscopy was carried out using a Olympus BX53M microscope equipped with a Olympus SC50 digital camera. The temperature was controlled *via* a HS1 Hot Stage Controller and a HS82 Hot Stage by Mettler Toledo. The ILCs were investigated under optical cross polarization using 4× and 10× magnifications. The compounds were deposited on a glass slide with a coverslip and heated to their respective transition temperatures.

### X-ray diffraction (XRD)

Small and wide angle X-ray measurements dependent on temperature were carried out with a Bruker AXS NanoStar X-ray diffractometer (CuKα-radiation with  $\lambda = 1.5418 \text{ \AA}$ ) equipped with a Vantec500 2D-detector and crossed Goebel mirrors. Further small angle X-ray measurements at ambient temperature were made with a Xeuss 3.0-system of Xenocs equipped with a GeniX<sup>3D</sup>  $\mu$ -source (CuKα-radiation with  $\lambda = 1.5418 \text{ \AA}$ ) and a Eiger2 R 1 M detector from Dectris Ltd. All samples for X-ray diffraction (SAXS and WAXS) were filled into Mark capillaries with a 0.7 mm outside diameter from Fa. Hilgenberg GmbH.

### Cyclic voltammetry (CV)

CV measurements were performed using the three-electrode system of a Metrohm Autolab PGSTAT204 and the TSC 70 closed measuring cell by rhd instruments. The CV cell consisted of platinum wires as the working ( $A = 4.9 \times 10^{-4} \text{ cm}^2$ ) and reference electrodes and a platinum crucible as the counter electrode. Before measurements, the ILCs were dried *in vacuo* (10<sup>−2</sup> mbar, T = r.t.) overnight. Afterwards the samples were dissolved in dry acetonitrile (0.05 M) and the solution was deoxygenated by bubbling nitrogen through the solution. Ferrocene was utilized as the internal standard

( $5 \times 10^{-4} \text{ M}$ ) and tetra-*n*-butylammonium hexafluorophosphate (Bu<sub>4</sub>NPF<sub>6</sub>) as the electrolyte (0.1 M). A scan rate of 0.1 V s<sup>−1</sup> and three subsequent scans were used for all measurements. The ferrocene half wave potentials were normalized to 0.0 V. For data analysis, the second scan of the measurements and a cut-off current of  $4 \times 10^{-7} \text{ A}$  were used.

### Dielectric spectroscopy (DS)

Dielectric measurements were performed on a Novocontrol GmbH Alpha dielectric spectrometer covering the frequency and temperature ranges 10<sup>−1</sup>–10<sup>7</sup> Hz and −70 to 200 °C, respectively. The value of the ionic conductivity was taken from the frequency independent plateau region of the real part of each ionic conductivity spectrum. Representative  $\sigma'(\omega)$  vs.  $\omega$  plots can be found in Fig. S1 (ESI<sup>†</sup>). Stainless steel electrodes (diameter = 15 mm) with a fixed distance provided by a quartz ring were used for the studies of the ILCs. During the measurements, the temperature was controlled using a Novocool system using a nitrogen gas cryostat with an accuracy of 0.1 K.

### DFT calculations

The molecule geometry was first optimized at the PM6 (semi-empirical<sup>25</sup>) level, with the total molecular volume calculated by carrying out a single point calculation at the B3LYP 3-21G\*<sup>26–28</sup> level using Gaussian.<sup>29</sup> The volume of the hydrophobic portion of this molecule was estimated by calculating the molecular volume of undecane (once again using B3LYP 3-21G\*); for the purposes of our volume calculations, we included the methylene directly attached to the ammonium as part of the hydrophilic fragment, since this group experiences strong polarization from the attached cation.

## Results and discussion

All of the ILCs presented in this study were synthesized by a 1 : 1 acid–base reaction between the zwitterions (Fig. 1) and methanesulfonic or sulfuric acid. All ILCs were obtained on a gram scale. Attenuated total reflection infrared (ATR IR) spectra of the ILCs are shown in Fig. 2. These IR spectra are influenced by the vibrations of the respective anions, as they are quite different in appearance. Both anions (mesylate or hydrogen sulfate) contain an SO<sub>3</sub><sup>−</sup> functional group and distinguishing between vibrations stemming from the starting zwitterion and the anions is difficult, as bands for SO<sub>3</sub> and SO<sub>2</sub> vibrations can be overlapping. However, all compounds show vibration bands typical for sulfonated compounds.<sup>30</sup> For the mesylate based ILCs in-phase and out-of-phase SO<sub>3</sub>/SO<sub>2</sub> stretching vibrations are found as bands between 1259 and 1040 cm<sup>−1</sup>.<sup>30</sup> Hydrogen sulfate based ILCs show these vibrations as bands between 1257 and 1042 cm<sup>−1</sup>.<sup>31–34</sup> SO<sub>3</sub>-bending vibrations can also be seen at 559 cm<sup>−1</sup> (CH<sub>3</sub>SO<sub>3</sub><sup>−</sup>) and 574 cm<sup>−1</sup> (HSO<sub>4</sub><sup>−</sup>), respectively. Moreover, the mesylate based ILCs show a strong band around 780 cm<sup>−1</sup>, which is associated with C–S stretching vibrations, whereas the hydrogen sulfate based ILCs show an additional



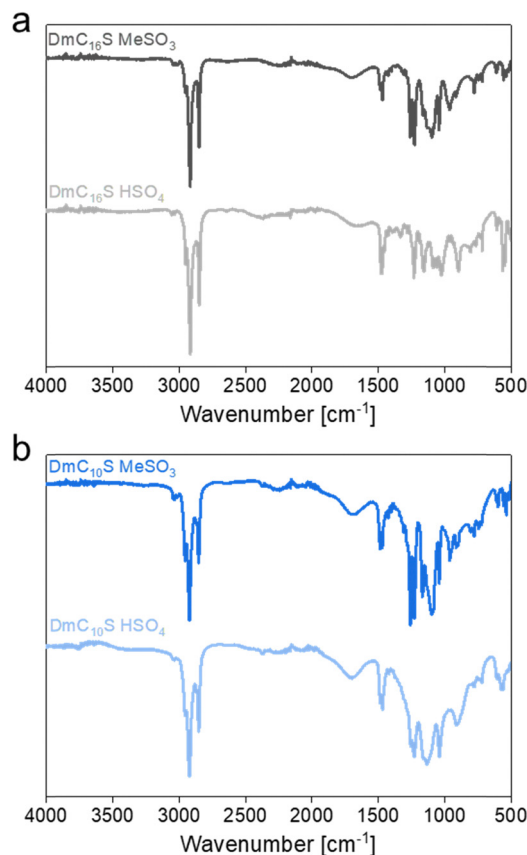


Fig. 2 Comparisons of the IR spectra of (a) DmC<sub>16</sub>S based ILCs and (b) DmC<sub>10</sub>S based ILCs.

band around 910 cm<sup>-1</sup>, caused by S-OH stretching of the hydroxyl entity in HSO<sub>4</sub><sup>-</sup>.<sup>30,33–35</sup>

Except for DmC<sub>16</sub>S HSO<sub>4</sub> all hydrogen sulfate containing ILCs show very broad bands in the IR spectra. This is not surprising as these ILCs are in their LC mesophase after synthesis (see Table 2 with the DSC data below) and broad IR bands might be the result of strong hydrogen bonding or cation–anion interactions or even anion–anion bonding in the ordered LC phase.<sup>34,36,37</sup> As hydrogen bonded systems can exhibit a variety of different bond lengths and bond angles with a range of different vibrational frequencies, the bands themselves broaden. Hydrogen sulfate anions are also known for forming HSO<sub>4</sub><sup>-</sup> chains or dimers.<sup>32,34,38,39</sup>

The thermal stability of electrolytes is a critical requirement for their safety and stability in electrochemical devices. Fig. 3 and Table 1 sum up the results of thermogravimetric analysis (TGA) measurements to determine the thermal stability of the ILCs.

All ILCs show a small mass loss between 0.2 and 1.4% up to 150 °C, which indicates a loss of residual methanol or moisture. Overall, all ILCs exhibit decomposition temperatures (with decomposition onset temperature  $T_{on}$  at a mass loss of 5%)<sup>40</sup> between 262 and 295 °C.  $T_{on}$  for the mesylate based ILCs are around 290 °C and therefore slightly higher than for the hydrogen sulfate based ILCs, which have  $T_{on}$  of around 275 °C. This is an interesting observation, as other studies on protic ILs have shown the opposite trend,<sup>36–42</sup> which is often explained by the strong

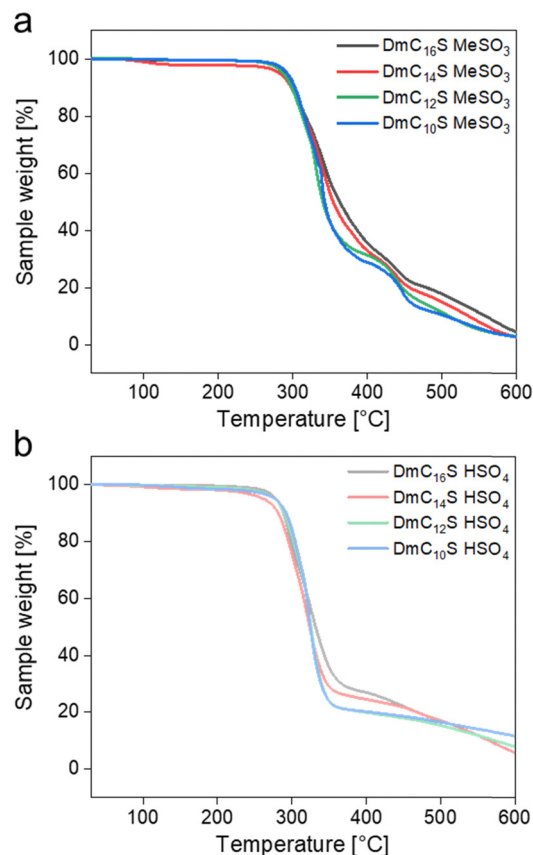


Fig. 3 TGA data of (a) mesylate based ILCs, and (b) hydrogensulfate based ILCs.

Table 1 Thermal properties of ILCs determined by TGA

	$T_{150}$ [%]	$T_{600}$ [%]	$T_{on}$ [°C]
DmC <sub>16</sub> S MeSO <sub>3</sub>	0.5	95.7	288.5
DmC <sub>14</sub> S MeSO <sub>3</sub>	1.0	93.8	295.1
DmC <sub>12</sub> S MeSO <sub>3</sub>	0.4	97.0	286.9
DmC <sub>10</sub> S MeSO <sub>3</sub>	0.4	97.2	292.5
DmC <sub>16</sub> S HSO <sub>4</sub>	0.2	94.2	279.0
DmC <sub>14</sub> S HSO <sub>4</sub>	1.4	94.1	262.1
DmC <sub>12</sub> S HSO <sub>4</sub>	0.6	92.0	277.4
DmC <sub>10</sub> S HSO <sub>4</sub>	0.9	88.3	277.6

$T_{on}$ : on-set decomposition temperature at 5% weight loss;  $T_{150}$ : weight loss in % at 150 °C;  $T_{600}$ : weight loss in % at 600 °C.

hydrogen bonding in hydrogen sulfate based ILs.<sup>34</sup> There seems to be no clear trend on whether hydrogen sulfate or mesylate based compounds exhibit higher thermal stabilities, as the current literature shows mixed information on this subject.<sup>40,41,43,44</sup>

This discrepancy – the fact that sometimes mesylates and sometime hydrogen sulfates show higher thermal stabilities – may be explained with the fact that these systems are (1) zwitterion-based providing a lot of additional interaction between the zwitterion, the mobile protons, and the anion, (2) highly hydrogen bonded both with the mesylate and the hydrogen sulfate anion,<sup>24</sup> and (3) also experiencing a complex interaction of the alkyl tails, which may lead to additional van der Waals interactions further affecting the local interactions



and mobilities. Overall, these ZI-based ILCs show a series of complementary and sometimes counteracting non-covalent interactions that make prediction of the relative thermal stabilities rather difficult.

The hydrogen sulfate based ILCs decompose in two ( $\text{DmC}_{10}\text{S HSO}_4$  and  $\text{DmC}_{12}\text{S HSO}_4$ ) or three ( $\text{DmC}_{14}\text{S HSO}_4$  and  $\text{DmC}_{16}\text{S HSO}_4$ ) steps. The first significant step shows a weight loss between 70–80% which ends between 355–370 °C. The second step for  $\text{DmC}_{10}\text{S HSO}_4$  and  $\text{DmC}_{12}\text{S HSO}_4$  is then a constant weight loss up to 600 °C. For  $\text{DmC}_{14}\text{S HSO}_4$  and  $\text{DmC}_{16}\text{S HSO}_4$  the second step up to 490 °C contains a small weight loss of around 8%, followed by a third step with a constant weight loss of up to 13%.

The thermal decomposition of the mesylate based ILCs occurs in three steps. The first weight loss occurring until 380–405 °C involves a sample loss of 65–70%. The second step of 13–20% sample weight loss can be seen up to 470 °C. The last decomposition step includes a weight loss of up to 17%. For all ILCs almost complete decomposition (88–97%) can be seen at 600 °C.

The thermal properties of the ILCs were further investigated by differential scanning calorimetry (DSC). Fig. 4 and Fig. S3 (ESI<sup>†</sup>) show the thermograms of the 2nd heating and cooling cycles for all compounds. The ILCs show a significantly

different behavior depending on the counter anion and the alkyl chain length. Indeed, a more complex thermal behavior for ILCs with longer chains has already been reported in the literature.<sup>45</sup> The shorter chained ILCs  $\text{DmC}_{12}\text{S MeSO}_3$ ,  $\text{DmC}_{10}\text{S MeSO}_3$ ,  $\text{DmC}_{14}\text{S HSO}_4$ ,  $\text{DmC}_{12}\text{S HSO}_4$  and  $\text{DmC}_{10}\text{S HSO}_4$  only show two processes upon 2nd heating and 2nd cooling – a glass transition and the transition from the mesophase into the isotropic liquid (Fig. S3, ESI<sup>†</sup>). The peak in the thermograms can therefore be identified as the isotropization temperature ( $T_{\text{iso}}$ , clearing point). Moreover, whereas the mesylate based compounds show delayed crystallization upon cooling, the hydrogen sulfate-based compounds remain in their LC state for months after cooling and storing in the laboratory at room temperature. Even when cooling to low temperatures in the DSC they remain in their LC state until  $T_g$ . This behavior has already been reported for some other LCs.<sup>15,46,47</sup> These LCs are called glassy LCs (GLCs) in the literature.<sup>15,46,48–50</sup>

$\text{DmC}_{16}\text{S MeSO}_3$  and  $\text{DmC}_{14}\text{S MeSO}_3$  both show (cold) crystallization and melting processes upon heating (Fig. 4a and d). However,  $\text{DmC}_{14}\text{S MeSO}_3$  exhibits one LC phase on heating which turns into the isotropic phase at around 120 °C and two LC phases on cooling (Fig. 4d). The second LC phase between 105–78 °C is therefore metastable, as it only appears upon cooling.<sup>18,51,52</sup> This behavior is also clearly seen in

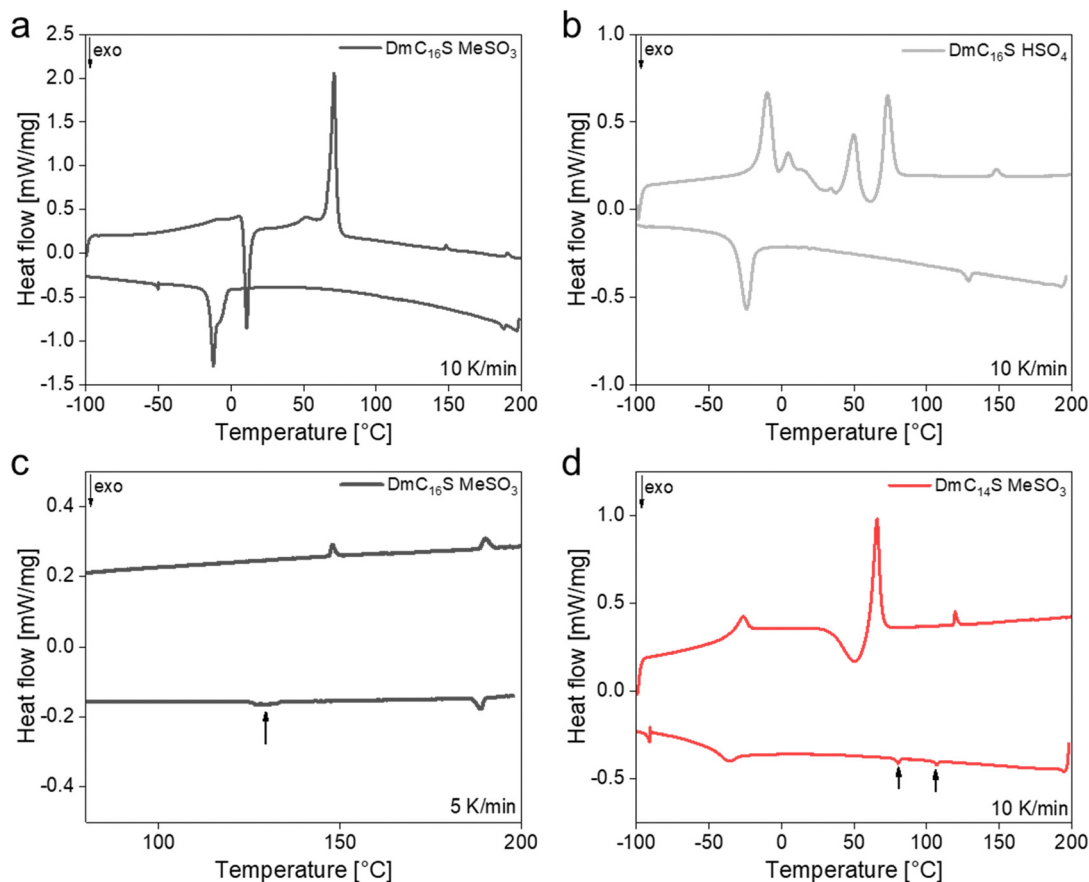


Fig. 4 2nd heating and cooling DSC runs for (a)  $\text{DmC}_{16}\text{S MeSO}_3$ , (b)  $\text{DmC}_{16}\text{S HSO}_4$ , and (c)  $\text{DmC}_{16}\text{S MeSO}_3$  with a heating/cooling rate of 5 K min<sup>-1</sup> (zoomed in to 80–200 °C), and (d)  $\text{DmC}_{14}\text{S MeSO}_3$ .



polarized optical microscopy (POM, Fig. S4, ESI†), as this phase cannot always be observed when the sample is cooled. In contrast to DmC<sub>14</sub>S MeSO<sub>3</sub>, DmC<sub>16</sub>S MeSO<sub>3</sub>, where the alkyl tail is longer by two carbon atoms, shows two mesophases upon heating and cooling. Both phases are therefore stable LC phases that can also clearly be observed *via* POM, see below. Both phases are, however, more clearly seen when slower heating/cooling rates are used (Fig. 4c).

The most complex thermal behavior is observed for DmC<sub>16</sub>S HSO<sub>4</sub>, Fig. 4b. Upon heating, this compound shows several cold crystallization and melting processes, suggesting the presence of various crystal structures and structural re-arrangements in the sample upon heating. The temperature window of the first mesophase (68–145 °C) is quite similar to that of DmC<sub>16</sub>S

MeSO<sub>3</sub>. The transition from the second mesophase into the isotropic phase, however, appears at a higher temperature ( $\geq 200$  °C) which is accompanied by the slow decomposition of the compound (as evidenced by TGA data, Fig. 3). Upon cooling DmC<sub>16</sub>S HSO<sub>4</sub> only shows the transition from the second into the first mesophase at around 125 °C and one crystallization process.

All relevant transition temperatures can be found in Table 2 and Fig. 5. When comparing  $T_{\text{iso}}$  of the shorter chained ILCs an influence of the ZI chain length can be observed. The shorter the chain on the zwitterion, the lower  $T_{\text{iso}}$  of the compound. This observation has already been described in the literature for several other ILs and ILCs.<sup>15,53–55</sup>

Furthermore, the hydrogen sulfate-based ILCs exhibit a broader mesophase window compared to the mesylate based

**Table 2** Phase transition temperatures (negative enthalpies  $\Delta H$  in kJ mol<sup>−1</sup>, if available) of ILCs

		DSC results of second heating/second cooling <sup>a</sup>			
		$T_g$	Cr-LC	LC <sub>1</sub> -LC <sub>2</sub>	LC-I
DmC <sub>16</sub> S MeSO <sub>3</sub>	Heating	−12.7	66.8 (−24.18)	147.2 (−0.26)	189.0 (−0.39)
	Cooling	—	−8.9 (19.67)	133.8 (0.32) <sup>c</sup>	189.2 (0.41)
DmC <sub>14</sub> S MeSO <sub>3</sub>	Heating	−35.4	60.8 (−9.04)	—	118.5 (−0.48)
	Cooling	−44.4	—	82.4 (0.24)	108.7 (0.17)
DmC <sub>12</sub> S MeSO <sub>3</sub>	Heating	−31.3	—	—	95.0 (−0.41)
	Cooling	−36.0	—	—	92.8 (0.43)
DmC <sub>10</sub> S MeSO <sub>3</sub>	Heating	−32.5	—	—	41.6 (−0.53)
	Cooling	−31.7	—	—	36.0 (0.52)
DmC <sub>16</sub> S HSO <sub>4</sub>	Heating	—	68.8 (−8.27) <sup>b</sup>	144.7 (−0.60)	> 200 °C Dec.
	Cooling	—	−18.5 (10.55)	131.2 (0.65)	> 200 °C Dec.
DmC <sub>14</sub> S HSO <sub>4</sub>	Heating	−34.3	—	—	> 200 °C Dec.
	Cooling	−48.6	—	—	> 200 °C Dec.
DmC <sub>12</sub> S HSO <sub>4</sub>	Heating	−25.8	—	—	195.1 (−0.68)
	Cooling	−26.0	—	—	> 200 °C (0.99)
DmC <sub>10</sub> S HSO <sub>4</sub>	Heating	−18.3	—	—	119.6 (−0.49)
	Cooling	−12.3	—	—	127.1 (0.47)

<sup>a</sup> LC<sub>1</sub>/LC<sub>2</sub>: 1st and 2nd mesophases in compounds DmC<sub>16</sub>S MeSO<sub>3</sub>, DmC<sub>14</sub>S MeSO<sub>3</sub> and DmC<sub>16</sub>S HSO<sub>4</sub>, Cr: crystalline, I: isotropic. <sup>b</sup> Value of last melting process. <sup>c</sup> Determined in measurement with a 5 K min<sup>−1</sup> cooling rate. Precise assignment of LC phases *via* POM and XRD described further below.

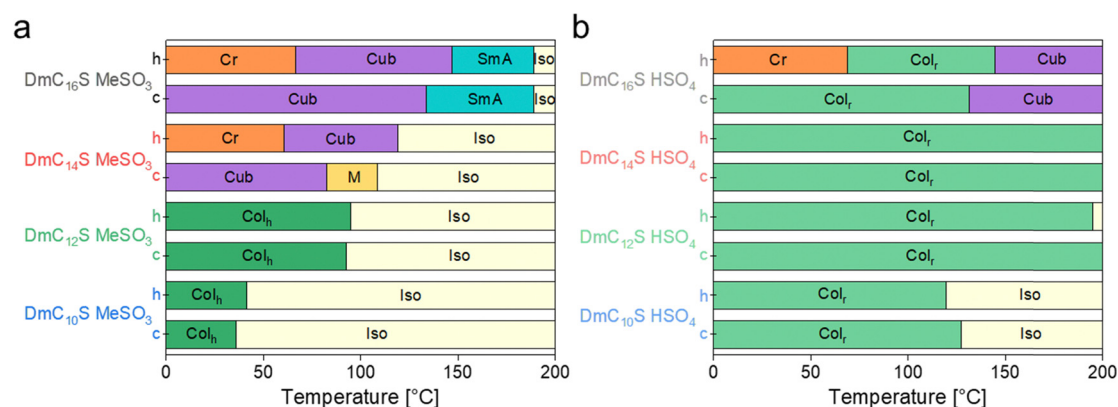


**Fig. 5** ILC phase transition temperatures of 2nd DSC heating (h) and cooling (c) runs for (a) mesylate based ILCs, and (b) hydrogen sulfate based ILCs.



ones; they only show a glass transition at around  $-12$  to  $-48$  °C and  $T_{\text{iso}}$  at around  $200$  °C. This might be due to the extensive hydrogen bond network associated with hydrogen sulfate based ILs and will be further discussed below. Overall, all phase transitions show very similar values upon heating and cooling and therefore only small hysteresis. Hysteresis of thermal transitions is a common observation for ILCs and is usually attributed to supercooling and/or high viscosity of the system.<sup>18,51,56,57</sup>

For a full assignment of the LC phases analysis *via* XRD measurements and POM is necessary. XRD analysis was conducted as WAXS and SAXS measurements, respectively, to assign the mesophase geometry. This analysis was more straightforward for the hydrogen sulfate based compounds, as all of these show a  $\text{Col}_r$  phase, with  $\text{DmC}_{16}\text{S HSO}_4$  exhibiting an additional cubic phase at higher temperatures. The  $\text{Col}_r$  phase of  $\text{DmC}_{16}\text{S HSO}_4$  hereby exhibits three sharp reflections at  $39.8$  Å,  $23.5$  Å, and  $20.5$  Å. The first reflection can be assigned as an overlapping of the two big reflections usually occurring in  $\text{Col}_r$  phases, which are (200) and (110).<sup>58</sup> The second reflection is then the (310) and the third again an overlapping of (400) and (220) with the lattice parameters  $a = 81.0$  Å and  $b = 45.3$  Å. The wide-angle measurements moreover show a broad halo, associated with the liquid-like disorder of the alkyl side chain in the ZIs. At higher temperatures  $\text{DmC}_{16}\text{S HSO}_4$  shows an altered diffraction pattern, which can be assigned to a Cub phase with reflections at  $37.6$  Å,  $24.7$  Å, and  $20.9$  Å, corresponding to the Miller indices of (200), (311), and (321) and a black POM image under crossed polarizers. The respective 2D diffractograms, integrated diffraction patterns and POM images are shown in Fig. 6. The presence of a cubic mesophase above a columnar one is quite peculiar, as the mesophase order is usually the

other way around.<sup>59–63</sup> However, there are some literature examples, where a cubic mesophase does indeed appear at higher temperatures than a columnar phase.<sup>64–66</sup>

The shorter chained hydrogen sulfate based ILCs all show reflections that can be assigned to the same Miller indices found for the lower temperature mesophase of  $\text{DmC}_{16}\text{S HSO}_4$ . However, these compounds show smaller lattice parameters, which is in agreement with the size of the respective ions (the shorter the chain-length of the cation the smaller the lattice parameters). The diffractogram of  $\text{DmC}_{10}\text{S HSO}_4$  only shows two clear reflections. This can be assigned to the less ordered nature of the system when the alkyl chain is shorter. We nevertheless assign the same mesophase to this compound based on the assignment of the longer chained ILCs and the respective POM images. All XRD assignments and values can be found in Table 3 and the respective POM images and diffraction patterns in Fig. 7 and Fig. S5, S6 (ESI†). The respective POM images show typical textures associated with a columnar mesophase, as they exhibit fan-shaped textures in the temperature windows corresponding with the  $\text{Col}_r$  phase.

The mesylate based ILCs show more complex behavior in both WAXS and SAXS, as we can overall find three different mesophases for these compounds: Cub,  $\text{Col}_h$ , and SmA. As can be seen in Fig. S6a and b (ESI†),  $\text{DmC}_{16}\text{S MeSO}_3$  exhibits a Cub phase at lower and SmA phase at higher temperatures. As for  $\text{DmC}_{16}\text{S HSO}_4$ , the cubic mesophase is characterized by a black POM image. The respective diffractogram shows reflections at  $37.6$  Å,  $32.6$  Å,  $20.3$  Å, and  $19.9$  Å, corresponding with the following indices: (211), (220), (331), and (421).

At higher temperatures,  $\text{DmC}_{16}\text{S MeSO}_3$  shows only one prominent reflection in the diffractogram, and the occurrence of a birefringent texture in the POM, indicating a SmA mesophase.

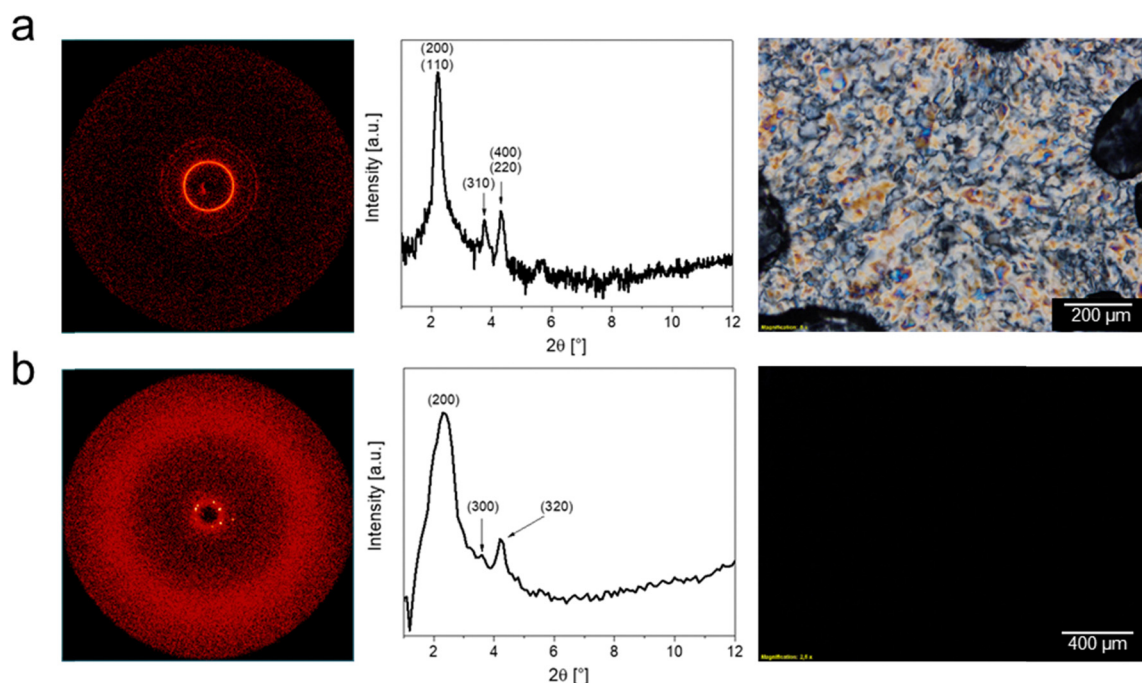


Fig. 6 Comparison of 2D diffraction patterns, integrated diffractograms and POM images for the two mesophases of  $\text{DmC}_{16}\text{S HSO}_4$  for (a)  $\text{Col}_r$  at  $45$  °C and (b) Cub at  $170$  °C.



Table 3 XRD results of sulfobetaine based ILCs

	Mesophase $T/^{\circ}\text{C}$	Reflections/ $\text{\AA}^{\circ}$ exp. (calc.)		Miller indices	Lattice parameters/ $\text{\AA}$
DmC <sub>16</sub> S MeSO <sub>3</sub>	Cub at 95 $^{\circ}\text{C}$	37.6	(37.4)	(211)	$a = 91.3$
		32.6	(32.3)	(220)	
		20.3	(21.0)	(331)	
		19.9	(19.9)	(421)	
		5.4		Halo	
DmC <sub>16</sub> S MeSO <sub>3</sub>	SmA at 170 $^{\circ}\text{C}$	34.4		(100)	$d = 34.4$
		5.5		Halo	
DmC <sub>14</sub> S MeSO <sub>3</sub>	Cub at 75 $^{\circ}\text{C}$	34.3	(34.5)	(211)	$a = 84.5$
		29.9	(29.9)	(220)	
		19.3	(19.4)	(331)	
		—	(18.4)	(421)	
		5.5		Halo	
DmC <sub>12</sub> S MeSO <sub>3</sub>	Col <sub>h</sub> at 20 $^{\circ}\text{C}$	30.6	(30.6)	(100)	$a = 35.3$
		17.6	(17.7)	(110)	
		15.3	(15.3)	(200)	
		5.4	(@60 $^{\circ}\text{C}$ )	Halo	
DmC <sub>10</sub> S MeSO <sub>3</sub>	Col <sub>h</sub> at 20 $^{\circ}\text{C}$	26.8	(26.8)	(100)	$a = 30.9$
		15.5	(15.5)	(110)	
		13.4	(13.4)	(200)	
		5.4		Halo	
DmC <sub>16</sub> S HSO <sub>4</sub>	Col <sub>r</sub> at 45 $^{\circ}\text{C}$	39.8	(40.5)	(200)	$a = 81.0$ $b = 45.5$
			(39.7)	(110)	
		23.5	(23.7)	(310)	
		20.5	(20.3)	(400)	
			(19.8)	(220)	
		5.4		Halo	
DmC <sub>16</sub> S HSO <sub>4</sub>	Cub at 170 $^{\circ}\text{C}$	37.6	(37.2)	(200)	$a = 74.4$
		24.7	(24.8)	(311)	
		20.9	(20.7)	(321)	
		5.5		Halo	
DmC <sub>14</sub> S HSO <sub>4</sub>	Col <sub>r</sub> at 75 $^{\circ}\text{C}$	35.6	(36.3)	(200)	$a = 72.5$ $b = 41.5$
			(36.0)	(110)	
		20.9	(20.9)	(310)	
		18.2	(18.1)	(400)	
			(18.0)	(220)	
		5.3		Halo	
DmC <sub>12</sub> S HSO <sub>4</sub>	Col <sub>r</sub> at 25 $^{\circ}\text{C}$	32.2	(32.5)	(200)	$a = 65.0$ $b = 37.5$
			(32.2)	(110)	
		19.2	(18.7)	(310)	
		16.5	(16.3)	(400)	
			(16.1)	(220)	
		4.8		Halo	
DmC <sub>10</sub> S HSO <sub>4</sub>	Col <sub>r</sub> at 25 $^{\circ}\text{C}$	28.7	(29.3)	(200)	$a = 57.5$ $b = 34.2$
			(29.1)	(110)	
		—	(16.9)	(310)	
		14.8	(14.6)	(400)	
			(14.5)	(220)	
		5.3		Halo	

While DmC<sub>14</sub>S MeSO<sub>3</sub> shows two phase transitions in the DSC cooling run, the mesophase at higher temperatures cannot be observed in the diffractograms at the respective temperature and only un-reliably while cooling under the microscope. This phase is therefore metastable and only the Cub phase is indeed a stable mesophase for this sample. In contrast to the longer chained compounds, the ILCs DmC<sub>12</sub>S MeSO<sub>3</sub> and DmC<sub>10</sub>S MeSO<sub>3</sub> (with their shorter alkyl chains) do not show a cubic, but a different mesophase, which is in agreement with the

literature.<sup>67</sup> DmC<sub>12</sub>S MeSO<sub>3</sub> and DmC<sub>10</sub>S MeSO<sub>3</sub> both exhibit a columnar hexagonal order, with the reflections corresponding to (100), (110), and (200) and fan-like textures in the POM images (Fig. 7 and Fig. S6, ESI†). When comparing the unit cell dimensions of the columnar mesophases with the ion sizes of the LC compounds, the unit cells show smaller dimensions than the respective ions. This can however be explained by the chemical structure of the cations, which consist mainly of long alkyl chains. These long alkyl chains can coil up and





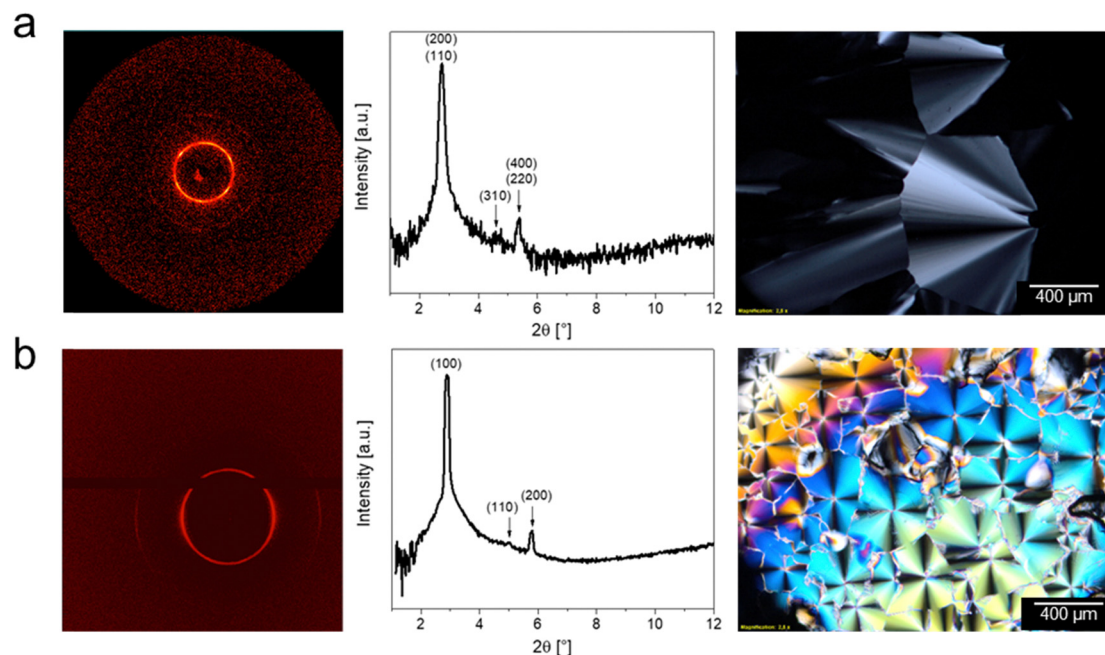


Fig. 7 Comparison of 2D diffraction patterns, diffractograms and POM images of  $C_{12}$  based ILCs (a)  $DmC_{12}S\ HSO_4$  at 25 °C, and (b)  $DmC_{12}S\ MeSO_3$  at 20 °C.

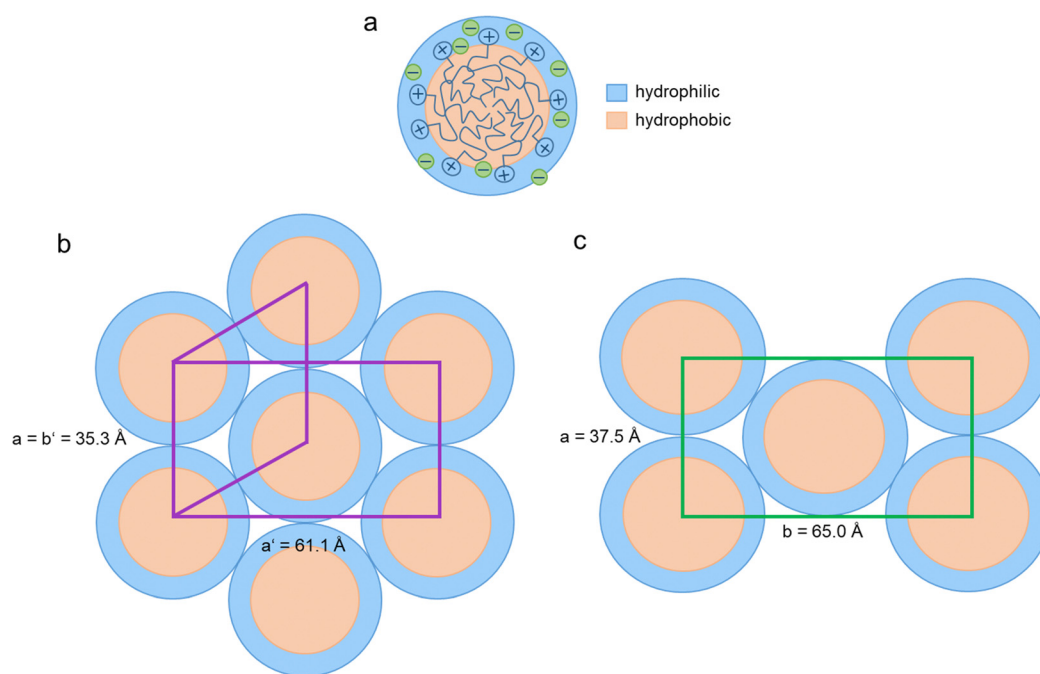


Fig. 8 (a) Sketch of the separation of ionic and hydrophobic parts. Comparison of packing models for (b)  $Col_h$  mesophase ( $DmC_{12}S\ MeSO_3$ ), and (c)  $Col_h$  mesophase ( $DmC_{12}S\ HSO_4$ ). Slight distortion in the hydrogen sulfate based ILCs leads to slightly larger unit cell parameters and a subsequent difference in the mesophase.

overlap and therefore the chains build a liquid-like ordered hydrophobic region in the middle of the column (see Fig. 8). This leads to smaller dimensions than expected by the sheer size of the ions.

Overall, all ILC mesophases are typical mesophases also described in the literature for other ILCs – zwitterionic<sup>61,68–71</sup>

and non-zwitterionic.<sup>45,60,63,72</sup> Interestingly, there are significant differences in the mesophase behavior between the hydrogen sulfate based and the mesylate based ILCs:

1. Broader temperature windows of the mesophases in the  $HSO_4$  based ILCs. These broader temperature windows and higher  $T_{iso}$  of the mesophases for the  $HSO_4$  based ILCs have



already been discussed above and are tentatively attributed to a presumably more extensive hydrogen bond network in these ILCs. Moreover, it has already been shown that smaller anions and longer alkyl chains can significantly increase  $T_{\text{iso}}$  in ILCs as electrostatic interactions have a significant influence on mesophase stability.<sup>45,59,67,69,70,73,74</sup> In the current case, the hydrogen sulfate anion is smaller than the mesylate anion and indeed the hydrogen sulfate based systems show higher  $T_{\text{iso}}$ .

2. A higher number of different mesophases for  $\text{MeSO}_3$  based ILCs. One possible explanation may be that a number of factors contribute to this behavior: (i) a slightly larger anion, (ii) a somewhat amphiphilic nature of the mesylate anion (as opposed to the hydrogen sulfate anion), and (iii) a lower number of hydrogen bonding sites due to the presence of the methyl group in the mesylate anion. In combination, these three effects may lead to higher structural flexibility in the mesylate based ILCs. This in turn may facilitate the formation of a larger number of ILC phases.

3. Different types of columnar mesophases even for shorter chained ILCs ( $\text{Col}_h$  vs.  $\text{Col}_r$ , see Fig. 7). Fig. 8 shows a packing model for both  $\text{DmC}_{12}\text{S}$  based compounds. Overall, the dimensions of the unit cells are quite similar for both compounds. We tentatively attribute the slight distortion to the presence of the methyl group in the mesylate anion and therefore differences in hydrogen-bonding and overall ionic and hydrophobic interactions. Possibly, the mesylate anion resides in the ionic section and in the more hydrophobic section, while the hydrogen sulfates are predominantly located in the ionic section of the ILCs. A wide hydrogen-bonding network associated with the hydrogen sulfate anions along the columns, but also between neighboring columns, may increase the volume fraction of the hydrophilic domains and therefore lead to the slight distortion between the  $\text{Col}_r$  and  $\text{Col}_h$  arrangements.

In order to support the model shown in Fig. 8 with the ionic domains on the outside of the columns we have performed DFT calculations of  $\text{DmC}_{12}\text{S MeSO}_3$ . The image below (Fig. 9) shows the ball and stick (a) and space filling model (b); the hydrophilic portion – including the methanesulfonic acid – is shown in blue, while the hydrophobic chain is shown in salmon (pink). The partial molecular volume of the hydrophilic group (*i.e.* hydrophobic: total volume) was calculated to be 0.40. Therefore, in the  $\text{C}_{10}$  and  $\text{C}_{12}$  derivatives, the hydrophobic chain occupies an appreciably smaller volume than the hydrophilic section, and hence should reside in the center of the column. As this chain increases in length, its size approaches that of the hydrophilic portion, the columnar nanostructure is replaced first with the cubic phase ( $\text{C}_{14}$ ), followed by the lamellar phase. If the situation was reversed, *i.e.* the hydrophobic volume was larger in the case of the  $\text{C}_{10}$  and  $\text{C}_{12}$ , increasing the chain length would not push the mesogens into the regime of cubic and lamellar phases; they would remain columnar. Thus, the volume calculations are fully consistent with the series trend. Note that the charged groups are moreover able to interact strongly when they are on the exterior of the column, since they are surrounded by other charged groups from both the same column and neighboring column.

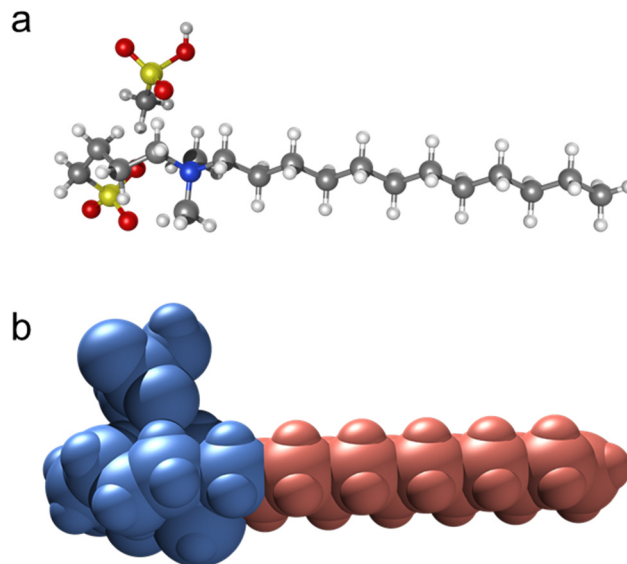


Fig. 9 DFT calculation results for  $\text{DmC}_{12}\text{S MeSO}_3$ : (a) ball and stick model, and (b) space filling model (blue: hydrophilic portion including the anion, salmon: hydrophobic alkyl tail).

The electrochemical behavior of the ILCs was furthermore investigated by cyclic voltammetry (CV) to determine the electrochemical stability window ( $\Delta E_{\text{W}} = E_{\text{anodic}} - E_{\text{cathodic}}$ ).  $\Delta E_{\text{W}}$  is defined as the region where no noteworthy faradaic current is observed in the voltammogram.<sup>75–77</sup> CV is therefore an important tool to assess their applicability for *e.g.* electrochemical devices.

Fig. 10 shows the voltammograms of all ILCs (except the  $\text{DmC}_{16}\text{S}$  compounds) grouped by anion (a, b) and a comparison between the two  $\text{DmC}_{12}\text{S}$  based ILCs (c). All voltammograms, independent of the anion, show a clear reduction process starting around  $-0.5$  to  $0.6$  V. This process can be assigned to the reduction of the cation, *i.e.*, the reduction of protons, which is a typical process for protic ILs.<sup>78–80</sup> Overall, the mesylate based ILCs show a slightly higher stability towards reduction compared to the hydrogen sulfate based ILCs. This has already been observed by Shmukler *et al.* for diethylammonium (DEA) based ILs,<sup>42</sup> whereas they found the opposite trend for ILs containing the triethylammonium (TEA) cation.<sup>43</sup> Moreover, Rana *et al.* found ILs based on the mesylate anion to also have one of the highest stabilities towards reduction in a series of similar ILs (with mesylate, triflate, bistriflimide anions).<sup>78</sup>

An analogous observation can be made for the anodic side of the voltammograms. Here, the mesylate-based compounds show a higher stability (of up to  $+0.15$  V) towards oxidation. The mesylate anion has already been reported to be rather stable towards oxidation and is often one of the most stable anions in a series of protic ILs.<sup>43,81</sup> In spite of this, for the aforementioned IL diethylammonium mesylate its hydrogen sulfate based counterpart showed higher oxidation stability.<sup>42</sup>

Generally speaking, however, oxidative processes around  $+1.4$ – $1.6$  V for the ILCs investigated in this study are in good agreement with results published for other protic ILs based on the same anions.<sup>40,42,43,82,83</sup> Overall, the size or composition of the ZIs in this study do not seem to influence the electrochemical stability,



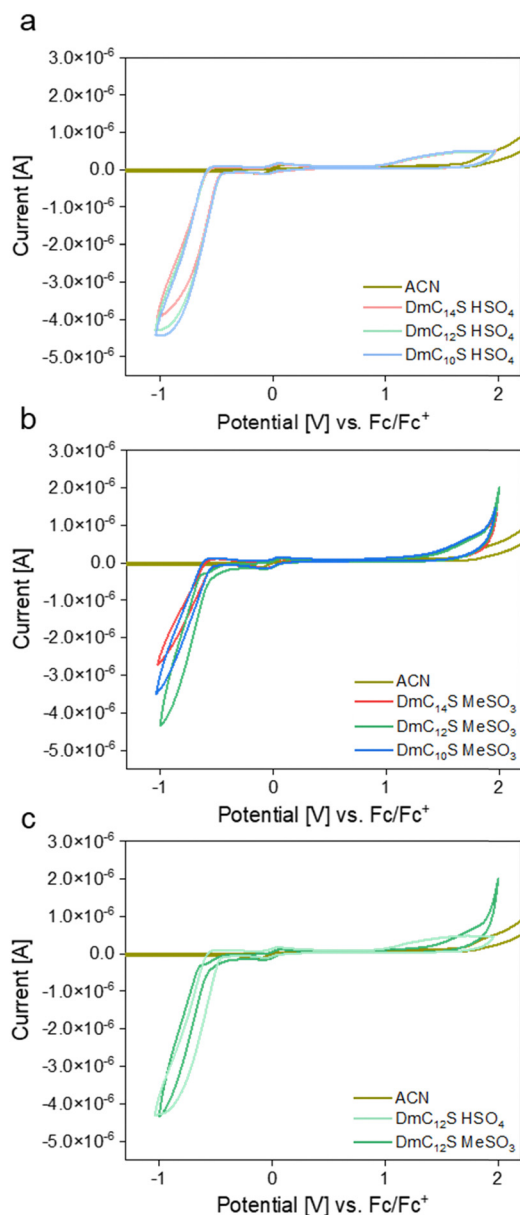


Fig. 10 Cyclic voltammograms of (a) hydrogensulfate based ILCs, (b) mesylate based ILCs, and (c) a comparison of DmC<sub>12</sub>S based ILCs.

whereas the anion has a slight influence on both the stability towards oxidation and towards reduction (see Table 4). Therefore, the mesylate based ILCs show slightly wider  $\Delta$ EW, with the most stable compound being DmC<sub>14</sub>S MeSO<sub>3</sub>. In general, the  $\Delta$ EW of the ILCs investigated in this study are comparable to those found for other protic ILCs.<sup>40,41,43,84</sup>

The ionic conductivities of the ILCs were analyzed *via* broadband dielectric spectroscopy (DS). Table 5 shows the conductivities of all ILCs at three different temperatures. As the ILCs show quite different phase behavior and mesophase types over varying temperature windows, a straightforward comparison of ionic conductivities by simply comparing the data for one specific temperature is not easily possible. Therefore, Table 5 shows the

Table 4 Electrochemical stability windows of ILCs<sup>a</sup> and solvent

Compound	Potential limits [V vs. Fc/Fc <sup>+</sup> ]		$\Delta$ EW [V]
	Anodic	Cathodic	
ACN	1.87	−2.40	4.27
DmC <sub>14</sub> S MeSO <sub>3</sub>	1.56	−0.60	2.16
DmC <sub>12</sub> S MeSO <sub>3</sub>	1.59	−0.54	2.13
DmC <sub>10</sub> S MeSO <sub>3</sub>	1.54	−0.60	2.14
DmC <sub>14</sub> S HSO <sub>4</sub>	1.45	−0.51	1.96
DmC <sub>12</sub> S HSO <sub>4</sub>	1.43	−0.50	1.93
DmC <sub>10</sub> S HSO <sub>4</sub>	1.40	−0.50	1.90

<sup>a</sup> DmC<sub>16</sub>S MeSO<sub>3</sub> and DmC<sub>16</sub>S HSO<sub>4</sub> were not measured as they show limited solubility in the CV measuring solution.

Table 5 Ionic conductivities of ILCs at different temperatures. Indices: Cub = cubic mesophase, Col<sub>r</sub> = columnar rectangular mesophase, Col<sub>h</sub> = columnar hexagonal mesophase, I = isotropic liquid

	$\sigma_{20^\circ\text{C}}$ [S cm <sup>−1</sup> ]	$\sigma_{90^\circ\text{C}}$ [S cm <sup>−1</sup> ]	$\sigma_{150^\circ\text{C}}$ [S cm <sup>−1</sup> ]
DmC <sub>16</sub> S MeSO <sub>3</sub>	$5.3 \times 10^{-13}$ Cub	$3.7 \times 10^{-8}$ Cub	$3.2 \times 10^{-6}$ SmA
DmC <sub>14</sub> S MeSO <sub>3</sub>	$1.0 \times 10^{-9}$ Cub	$2.4 \times 10^{-6}$ Cub	$1.3 \times 10^{-4}$ I
DmC <sub>12</sub> S MeSO <sub>3</sub>	$4.8 \times 10^{-8}$ Col <sub>h</sub>	$2.5 \times 10^{-5}$ Col <sub>h</sub>	$5.1 \times 10^{-4}$ I
DmC <sub>10</sub> S MeSO <sub>3</sub>	$1.8 \times 10^{-7}$ Col <sub>h</sub>	$5.6 \times 10^{-5}$ I	$6.7 \times 10^{-4}$ I
DmC <sub>16</sub> S HSO <sub>4</sub>	$1.9 \times 10^{-7}$ Col <sub>r</sub>	$3.0 \times 10^{-5}$ Col <sub>r</sub>	$2.6 \times 10^{-4}$ Cub
DmC <sub>14</sub> S HSO <sub>4</sub>	$2.9 \times 10^{-7}$ Col <sub>r</sub>	$3.6 \times 10^{-5}$ Col <sub>r</sub>	$3.0 \times 10^{-4}$ Col <sub>r</sub>
DmC <sub>12</sub> S HSO <sub>4</sub>	$1.6 \times 10^{-7}$ Col <sub>r</sub>	$3.1 \times 10^{-5}$ Col <sub>r</sub>	$3.2 \times 10^{-4}$ Col <sub>r</sub>
DmC <sub>10</sub> S HSO <sub>4</sub>	$1.1 \times 10^{-6}$ Col <sub>r</sub>	$1.2 \times 10^{-4}$ Col <sub>r</sub>	$1.1 \times 10^{-3}$ I

ionic conductivities at room temperature (20 °C), 90 °C and 150 °C. Indices denote the state of the compounds at the respective temperature.

Fig. 11 shows the ionic conductivities *vs.* 1000 T<sup>−1</sup> for all ILCs. Overall, the ionic conductivities increase with increasing temperature and also clearly show the respective phase transitions (Fig. S7, ESI†). The mesylate-based ILCs hereby show a clear dependency of the ionic conductivity on chain-length. The conductivities decrease with increasing chain length of the ZIs. However, the differences in conductivity are more pronounced when the chains get longer, as the values for DmC<sub>12</sub>S MeSO<sub>3</sub> and DmC<sub>10</sub>S MeSO<sub>3</sub> are quite similar. The pronounced differences in the conductivities might therefore not only be explained by the increase in chain length, but more importantly by the mesophase type of the respective ILCs. As the two shorter chained ILCs both exhibit a Col<sub>h</sub> mesophase, their ionic conductivities are less influenced by the differences in chain length, as the ion conduction inside the mesophase could appear along the columns, independent on the size of the ZI. The differences in chain length do, however, have an influence on the conductivity in the Cub phases exhibited by DmC<sub>16</sub>S MeSO<sub>3</sub> and DmC<sub>14</sub>S MeSO<sub>3</sub>. Here, the longer chain seems to significantly influence the possible conduction pathways, as the longer chains expand the overall hydrophobic domains and might therefore limit possibilities for conduction.

Overall, the hydrogen sulfate-based ILCs in their Col<sub>r</sub> mesophase show slightly higher ionic conductivities than their mesylate-based counterparts (Fig. S7, ESI†). Moreover, the chain lengths of the ZIs do not show such an influence as for the mesylate ILCs. All three longer chained hydrogen sulfate-based ILCs exhibit almost equal ionic conductivities. This



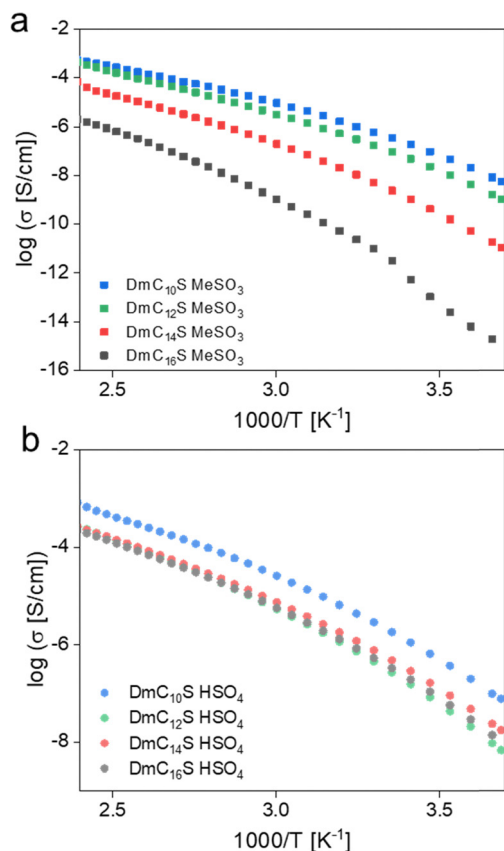


Fig. 11 Ionic conductivities of (a) mesylate based ILCs, and (b) hydrogensulfate based ILCs from room temperature to elevated temperatures.

suggests that the bulk conductivity measured for these systems is not significantly influenced by the chain length, as conduction seems to arise along the columns, as previously seen for DmC<sub>12</sub>S MeSO<sub>3</sub> and DmC<sub>10</sub>S MeSO<sub>3</sub>. It is therefore independent of the actual size of the cation structure. This is in agreement with the results found by DSC measurements, where all three long chained ILCs show similar behavior and high  $T_{\text{iso}}$ . Moreover, it has already been shown in the literature that longer alkyl chains do not always correspond with lower ionic conductivities.<sup>45</sup> DmC<sub>10</sub>S HSO<sub>4</sub>, however, shows a higher conductivity than the longer-chained compounds. This is in agreement with a slightly different phase behavior in the form of lower  $T_{\text{iso}}$  found *via* DSC. One possible explanation might be that DmC<sub>10</sub>S HSO<sub>4</sub> is the last representative in the hydrogen sulfate group to show LC behavior (with DmC<sub>8</sub>S HSO<sub>4</sub> being liquid) and might therefore already experience significantly less intermolecular interactions and lower viscosity, lowering  $T_{\text{iso}}$  but increasing the conductivity. Overall, DmC<sub>10</sub>S HSO<sub>4</sub> exhibits the highest conductivities over the temperature range investigated. However, the highest ionic conductivity in an LC phase at 150 °C is observed for DmC<sub>12</sub>S HSO<sub>4</sub>.

The literature is not conclusive in regards to comparisons of ionic conductivities of mesylate and hydrogen sulfate-based compounds. For example, Shmukler *et al.* found higher conductivities for a series of TEA based ILs with mesylate compared to hydrogen sulfate as the anion,<sup>43</sup> whereas they made the

opposite observation for DEA based ILs and the same anions.<sup>42</sup> However, the ionic conductivities found for the zwitterionic ILCs of this study are comparable with other (zwitterionic) ILCs found in the literature.<sup>45,59,62,85</sup> Soberats *et al.* described sulfobetaine-based ILCs that showed a maximum conductivity of 10<sup>−4</sup> S cm<sup>−1</sup> in the cubic phase at 130 °C.<sup>71</sup> ILCs based on a long-chained benzoic acid and sulfobetaine zwitterions were reported by Qiao *et al.* They found higher conductivities for shorter zwitterions with a maximum conductivity of 10<sup>−5</sup> S cm<sup>−1</sup> at 110 °C in the lamellar phase.<sup>69</sup>

All ILCs clearly show non-Arrhenius behavior for their conductivities. This is illustrated by a curvature in the graphs showing a non-linear dependence of conductivity on inverse temperature, as can be clearly seen in figure sigma (Fig. 11). This non-Arrhenius behavior is characterized by a curvature of the graphs, which has been observed for many ILs and ILCs.<sup>55,86–89</sup> The conductivity of all ILCs is therefore best described with the Vogel–Fulcher–Tamann (VFT) relationship (eqn (1)).<sup>90–92</sup> In this equation,  $\sigma_0$  represents the maximum conductivity at infinite temperature,  $T_0$  is the ideal glass transition temperature and  $B$  is the pseudo activation energy (or an adjustable parameter).  $B$  is hereby related to segmental mobility as the dependence of the conductivity on the VFT equation suggests a liquid-like nature of the system and activation energies that are more dependent on segmental or side relaxation dynamics than elastic or electrostatic contributions.<sup>93–96</sup>

The results of the VFT fitting can be found in Table 6 and representative VFT fits for DmC<sub>16</sub>S HSO<sub>4</sub>, DmC<sub>12</sub>S HSO<sub>4</sub> and DmC<sub>12</sub>S MeSO<sub>3</sub> are shown in Fig. S8 (ESI†). It is hereby noteworthy that for DmC<sub>16</sub>S HSO<sub>4</sub> and DmC<sub>16</sub>S MeSO<sub>3</sub> two individual VFT plots were used, as these ILC exhibit two mesophases.

$$\sigma = \sigma_0 \exp \left[ \frac{-B}{T - T_0} \right] \quad (1)$$

When comparing the  $B$  values in Table 6 the same observations as already seen for the conductivities can be made. For the mesylate-based compounds comparison of the  $B$  values is not straightforward, as  $B$  is determined in different mesophases. Overall though,  $B$  is lower for shorter chains and more or less follows the trend  $C_{16} \approx C_{14} > C_{12} > C_{10}$ , with DmC<sub>10</sub>S MeSO<sub>3</sub> showing the smallest pseudo activation energy of all ILCs studied here. For the hydrogen sulfate-based ILCs all  $B$

Table 6 VFT fitting results obtained at different temperatures in different LC phases

	$\sigma_0$ [S cm <sup>−1</sup> ]	$B$ [K]	$T_0$ [K]	LC
DmC <sub>16</sub> S MeSO <sub>3</sub>	$2.1 \times 10^{-2}$	738.2	235.0	SmA
	$1.5 \times 10^1$	1734.4	162.4	Cub
DmC <sub>14</sub> S MeSO <sub>3</sub>	$2.7 \times 10^{-0}$	1196.1	166.0	Cub
DmC <sub>12</sub> S MeSO <sub>3</sub>	$5.3 \times 10^{-1}$	799.6	179.5	Col <sub>h</sub>
DmC <sub>10</sub> S MeSO <sub>3</sub>	$1.0 \times 10^{-1}$	600.2	188.4	Col <sub>h</sub>
DmC <sub>16</sub> S HSO <sub>4</sub>	$1.7 \times 10^{-0}$	1193.7	109.9	Cub
	$3.2 \times 10^{-1}$	800.1	164.4	Col <sub>r</sub>
DmC <sub>14</sub> S HSO <sub>4</sub>	$1.7 \times 10^{-1}$	707.6	170.3	Col <sub>r</sub>
DmC <sub>12</sub> S HSO <sub>4</sub>	$2.7 \times 10^{-1}$	746.5	173.3	Col <sub>r</sub>
DmC <sub>10</sub> S HSO <sub>4</sub>	$3.4 \times 10^{-1}$	664.6	171.1	Col <sub>r</sub>





values with the exception of DmC<sub>16</sub>S HSO<sub>4</sub> in the Cub phase are quite similar. This again hints at the formation of the same mesophase, as already discussed above. All pseudo activation energies for the ILCs in this study are comparable with values found for other ILCs or ILs analyzed *via* VFT fitting.<sup>41,96–98</sup>

## Conclusion

New zwitterion based ILCs can be synthesized in fairly large amounts using a simple protocol. The resulting ILCs show a rather complex phase behavior and the nature of the counter ion and the length of the alkyl chain are two main influences controlling this phase behavior. Somewhat surprisingly the most likely arrangement of the ILC molecules in the columnar phases has the ionic groups on the outside of the columns and the alkyl tails in the centers. Possibly, this arrangement contributes to the relatively good ionic conductivities observed for these compounds. This also suggests that the major structure controlling interactions are the ionic forces of the hydrophilic part and not the alkyl tails. The ILCs are stable up to slightly above 200 °C and show an electrochemical stability window of around 2 V. As a result, these materials are promising candidates for ion or proton conduction.

## Data availability

The data that supports the findings of this study are available in the ESI,<sup>†</sup> of this article.

## Conflicts of interest

There are no conflicts to declare.

## Acknowledgements

The authors gratefully acknowledge financial support by the Deutsche Akademische Austauschdienst (DAAD) – Forschungstipendien für Doktorandinnen und Doktoranden 2021/2022 (57556280), University of Potsdam (grant # 53170000), and Deutsche Forschungsgemeinschaft (DFG, grant # TA571/16-2, Gi 243/8-2), the National Science Centre, Poland (grant number Opus 21, 2021/41/B/ST5/00840), and the Natural Sciences and Engineering Research Council of Canada (NSERC GRANT RGPIN-2022-03548). The authors thank A. Nitschke (University of Potsdam) for help with TGA experiments.

## References

- O. Danyliv and A. Martinelli, Nafion/Protic Ionic Liquid Blends: Nanoscale Organization and Transport Properties, *J. Phys. Chem. C*, 2019, **123**(23), 14813–14824, DOI: [10.1021/acs.jpcc.9b02874](#).
- U. A. Rana, M. Forsyth, D. R. MacFarlane and J. M. Pringle, Toward protic ionic liquid and organic ionic plastic crystal electrolytes for fuel cells, *Electrochim. Acta*, 2012, **84**, 213–222, DOI: [10.1016/j.electacta.2012.03.058](#).
- V. M. Ortiz-Martínez, A. Ortiz, V. Fernández-Stefanuto, E. Tojo, M. Colpaert, B. Améduri and I. Ortiz, Fuel cell electrolyte membranes based on copolymers of protic ionic liquid [HSO<sub>3</sub>-BVIm][TfO] with MMA and hPFSVE, *Polymer*, 2019, **179**, 121583, DOI: [10.1016/j.polymer.2019.121583](#).
- S.-Y. Lee, A. Ogawa, M. Kanno, H. Nakamoto, T. Yasuda and M. Watanabe, Nonhumidified intermediate temperature fuel cells using protic ionic liquids, *J. Am. Chem. Soc.*, 2010, **132**(28), 9764–9773, DOI: [10.1021/ja102367x](#).
- T. Torimoto, T. Tsuda, K. Okazaki and S. Kuwabata, New frontiers in materials science opened by ionic liquids, *Adv. Mater.*, 2010, **22**(11), 1196–1221, DOI: [10.1002/adma.200902184](#).
- S. Werner, M. Haumann and P. Wasserscheid, Ionic liquids in chemical engineering, *Annu. Rev. Chem. Biomol. Eng.*, 2010, **1**, 203–230, DOI: [10.1146/annurev-chembioeng-073009-100915](#).
- K. Binnemans, Ionic liquid crystals, *Chem. Rev.*, 2005, **105**(11), 4148–4204, DOI: [10.1021/cr0400919](#).
- T. Ichikawa, T. Kato and H. Ohno, Dimension control of ionic liquids, *Chem. Commun.*, 2019, **55**(57), 8205–8214, DOI: [10.1039/C9CC04280F](#).
- T. L. Greaves and C. J. Drummond, Protic ionic liquids: properties and applications, *Chem. Rev.*, 2008, **108**(1), 206–237, DOI: [10.1021/cr068040u](#).
- T. L. Greaves, H. Broomhall, A. Weerawardena, D. A. Osborne, B. A. Canonge and C. J. Drummond, How ionic species structure influences phase structure and transitions from protic ionic liquids to liquid crystals to crystals, *Faraday Discuss.*, 2017, **206**, 29–48, DOI: [10.1039/c7fd00148g](#).
- S. J. Devaki and R. Sasi, Ionic Liquids/Ionic Liquid Crystals for Safe and Sustainable Energy Storage Systems, in *Progress and Developments in Ionic Liquids*, ed. S. Handy, InTech, 2017, DOI: [10.5772/65888](#).
- T. Ichikawa, Zwitterions as building blocks for functional liquid crystals and block copolymers, *Polym. J.*, 2017, **49**(5), 413–421, DOI: [10.1038/pj.2017.6](#).
- B. Soberats, E. Uchida, M. Yoshio, J. Kagimoto, H. Ohno and T. Kato, Macroscopic photocontrol of ion-transporting pathways of a nanostructured imidazolium-based photoresponsive liquid crystal, *J. Am. Chem. Soc.*, 2014, **136**(27), 9552–9555, DOI: [10.1021/ja5041573](#).
- N. Yamanaka, R. Kawano, W. Kubo, T. Kitamura, Y. Wada, M. Watanabe and S. Yanagida, Ionic liquid crystal as a hole transport layer of dye-sensitized solar cells, *Chem. Commun.*, 2005, (6), 740–742, DOI: [10.1039/B417610C](#).
- T. Kobayashi, T. Ichikawa, T. Kato and H. Ohno, Development of Glassy Bicontinuous Cubic Liquid Crystals for Solid Proton-Conductive Materials, *Adv. Mater.*, 2017, **29**(4), 1604429, DOI: [10.1002/adma.201604429](#).
- T. Mukai, M. Yoshio, T. Kato, M. Yoshizawa-Fujita and H. Ohno, Self-organization of Protonated 2-heptadecylimidazole as an Effective Ion Conductive Matrix, *Electrochemistry*, 2005, **73**(8), 623–626, DOI: [10.5796/electrochemistry.73.623](#).
- T. Mukai, M. Yoshio, T. Kato and H. Ohno, Self-assembled N-Alkylimidazolium Perfluorooctanesulfonates, *Chem. Lett.*, 2005, **34**(3), 442–443, DOI: [10.1246/cl.2005.442](#).





- 18 K. Goossens, K. Lava, C. W. Bielawski and K. Binnemans, Ionic Liquid Crystals: Versatile Materials, *Chem. Rev.*, 2016, **116**(8), 4643–4807, DOI: [10.1021/cr400334b](#).
- 19 S. Ueda, J. Kagimoto, T. Ichikawa, T. Kato and H. Ohno, Anisotropic proton-conductive materials formed by the self-organization of phosphonium-type zwitterions, *Adv. Mater.*, 2011, **23**(27), 3071–3074, DOI: [10.1002/adma.201100942](#).
- 20 T. Ichikawa, T. Kato and H. Ohno, 3D continuous water nanosheet as a gyroid minimal surface formed by bicontinuous cubic liquid-crystalline zwitterions, *J. Am. Chem. Soc.*, 2012, **134**(28), 11354–11357, DOI: [10.1021/ja304124w](#).
- 21 E. Delahaye, R. Göbel, R. Löbbecke, R. Guillot, C. Sieber and A. Taubert, Silica ionogels for proton transport, *J. Mater. Chem.*, 2012, **22**(33), 17140, DOI: [10.1039/c2jm00037g](#).
- 22 A. Taubert, R. Löbbecke, B. Kirchner and F. Leroux, First examples of organosilica-based ionogels: synthesis and electrochemical behavior, *Beilstein J. Nanotechnol.*, 2017, **8**, 736–751, DOI: [10.3762/bjnano.8.77](#).
- 23 K. Zehbe, A. Lange and A. Taubert, Stereolithography Provides Access to 3D Printed Ionogels with High Ionic Conductivity, *Energy Fuels*, 2019, **33**(12), 12885–12893, DOI: [10.1021/acs.energyfuels.9b03379](#).
- 24 Z. Wojnarowska, A. Lange, A. Taubert and M. Paluch, Ion and Proton Transport In Aqueous/Nonaqueous Acidic Ionic Liquids for Fuel-Cell Applications-Insight from High-Pressure Dielectric Studies, *ACS Appl. Mater. Interfaces*, 2021, **13**(26), 30614–30624, DOI: [10.1021/acsami.1c06260](#).
- 25 J. J. P. Stewart, Optimization of parameters for semiempirical methods V: modification of NDDO approximations and application to 70 elements, *J. Mol. Model.*, 2007, **13**(12), 1173–1213, DOI: [10.1007/s00894-007-0233-4](#).
- 26 A. D. Becke, Density-functional thermochemistry. III. The role of exact exchange, *J. Chem. Phys.*, 1993, **98**(7), 5648–5652, DOI: [10.1063/1.464913](#).
- 27 C. Lee, W. Yang and R. G. Parr, Development of the Colle-Salvetti correlation-energy formula into a functional of the electron density, *Phys. Rev. B: Condens. Matter Mater. Phys.*, 1988, **37**(2), 785–789, DOI: [10.1103/PhysRevB.37.785](#).
- 28 R. G. Parr and Y. Weitao, *Density-Functional Theory of Atoms and Molecules*, International Series of Monographs on Chemistry, Oxford University Press, ProQuest, 2015.
- 29 M. J. Frisch, G. W. Trucks, H. B. Schlegel, G. E. Scuseria, M. A. Robb, J. R. Cheeseman, G. Scalmani, V. Barone, G. A. Petersson, H. Nakatsuji, X. Li, M. Caricato, A. Marenich, J. Bloino, B. G. Janesko, R. Gomperts, B. Mennucci, H. P. Hratchian, J. V. Ortiz, A. F. Izmaylov, J. L. Sonnenberg, D. Williams-Young, F. Ding, F. Lipparini, F. Egidi, J. Goings, B. Peng, A. Petrone, T. Henderson, D. Ranasinghe, V. G. Zakrzewski, J. Gao, N. Rega, G. Zheng, W. Liang, M. Hada, M. Ehara, K. Toyota, R. Fukuda, J. Hasegawa, M. Ishida, T. Nakajima, Y. Honda, O. Kitao, H. Nakai, T. Vreven, K. Throssell, J. A. Montgomery Jr., J. E. Peralta, F. Ogliaro, M. Bearpark, J. J. Heyd, E. Brothers, K. N. Kudin, V. N. Staroverov, T. Keith, R. Kobayashi, J. Normand, K. Raghavachari, A. Rendell, J. C. Burant, S. S. Iyengar, J. Tomasi, M. Cossi, J. M. Millam, M. Klene, C. Adamo, R. Cammi, J. W. Ochterski, R. L. Martin, K. Morokuma, O. Farkas, J. B. Foresman and D. J. Fox, *Gaussian 09*, Gaussian, Inc., Gaussian, Wallingford CT, 2016.
- 30 P. Larkin, *Infrared and Raman spectroscopy: Principles and spectral interpretation*, 2nd edn, Elsevier, 2018.
- 31 M. Belhouchet, M. Bahri, J. M. Savariault and T. Mhiri, Structural and vibrational study of a new organic hydrogen sulfate, *Spectrochim. Acta, Part A*, 2005, **61**(3), 387–393, DOI: [10.1016/j.saa.2004.04.013](#).
- 32 A. B. Horn and K. Jessica Sully, ATR-IR spectroscopic studies of the formation of sulfuric acid and sulfuric acid monohydrate films, *Phys. Chem. Chem. Phys.*, 1999, **1**(16), 3801–3806, DOI: [10.1039/A904544I](#).
- 33 T. I. Yacovitch, T. Wende, L. Jiang, N. Heine, G. Meijer, D. M. Neumark and K. R. Asmis, Infrared Spectroscopy of Hydrated Bisulfate Anion Clusters:  $\text{HSO}_4^-(\text{H}_2\text{O})_{1-16}$ , *J. Phys. Chem. Lett.*, 2011, **2**(17), 2135–2140, DOI: [10.1021/jz200917f](#).
- 34 M. C. Ribeiro, Strong anion–anion hydrogen bond in the ionic liquid 1-ethyl-3-methylimidazolium hydrogen sulfate, *J. Mol. Liq.*, 2020, **310**, 113178, DOI: [10.1016/j.molliq.2020.113178](#).
- 35 A. Goypiro, J. de Villepin and A. Novak, Raman and infrared study of KHSO<sub>4</sub> 4 crystal, *J. Raman Spectrosc.*, 1980, **9**(5), 297–303, DOI: [10.1002/jrs.1250090505](#).
- 36 L. Cammarata, S. G. Kazarian, P. A. Salter and T. Welton, Molecular states of water in room temperature ionic liquids, *Phys. Chem. Chem. Phys.*, 2001, **3**(23), 5192–5200, DOI: [10.1039/B106900DESI](#),<sup>†</sup> available. See <https://www.rsc.org/suppdata/cp/b1/b106900d>.
- 37 J. Grondin, J.-C. Lassègues, D. Cavagnat, T. Buffeteau, P. Johansson and R. Holomb, Revisited vibrational assignments of imidazolium-based ionic liquids, *J. Raman Spectrosc.*, 2011, **42**(4), 733–743, DOI: [10.1002/jrs.2754](#).
- 38 M. C. C. Ribeiro, High viscosity of imidazolium ionic liquids with the hydrogen sulfate anion: a Raman spectroscopy study, *J. Phys. Chem. B*, 2012, **116**(24), 7281–7290, DOI: [10.1021/jp302091d](#).
- 39 L. F. O. Faria, T. A. Lima, F. F. Ferreira and M. C. C. Ribeiro, Ultraslow Phase Transitions in an Anion–Anion Hydrogen-Bonded Ionic Liquid, *J. Phys. Chem. B*, 2018, **122**(6), 1972–1980, DOI: [10.1021/acs.jpcc.7b09497](#).
- 40 C. Zhao, G. Burrell, A. A. J. Torriero, F. Separovic, N. F. Dunlop, D. R. MacFarlane and A. M. Bond, Electrochemistry of room temperature protic ionic liquids, *J. Phys. Chem. B*, 2008, **112**(23), 6923–6936, DOI: [10.1021/jp711804j](#).
- 41 L. E. Shmukler, I. V. Fedorova, Y. A. Fadeeva and L. P. Safonova, The physicochemical properties and structure of alkylammonium protic ionic liquids of  $\text{RnH}_{4-n}\text{NX}$  ( $n = 1-3$ ) family. A mini-review, *J. Mol. Liq.*, 2021, **321**, 114350, DOI: [10.1016/j.molliq.2020.114350](#).
- 42 L. E. Shmukler, Y. A. Fadeeva, N. M. Stel'makh and L. P. Safonova, Membranes Based on PVdF–HFP and Alkylammonium Protic Ionic Liquids: Thermal and Transport Properties, *Russ. J. Phys. Chem.*, 2023, **97**(1), 257–264, DOI: [10.1134/S0036024423010272](#).
- 43 L. E. Shmukler, M. S. Gruzdev, N. O. Kudryakova, Y. A. Fadeeva, A. M. Kolker and L. P. Safonova, Triethylammonium-



- based protic ionic liquids with sulfonic acids: Phase behavior and electrochemistry, *J. Mol. Liq.*, 2018, **266**, 139–146, DOI: [10.1016/j.molliq.2018.06.059](https://doi.org/10.1016/j.molliq.2018.06.059).
- 44 H. Nakamoto and M. Watanabe, Brønsted acid-base ionic liquids for fuel cell electrolytes, *Chem. Commun.*, 2007, (24), 2539–2541, DOI: [10.1039/B618953A](https://doi.org/10.1039/B618953A).
  - 45 D. Kuo, B. Soberats, K. R. S. Kumar, M. Yoshio, T. Ichikawa, H. Ohno, X. Zeng, G. Ungar and T. Kato, Switching of ionic conductivities in columnar liquid-crystalline anilinium salts: effects of alkyl chains, ammonium cations and counter anions on thermal properties and switching temperatures, *Mol. Syst. Des. Eng.*, 2019, **4**(2), 342–347, DOI: [10.1039/c8me00099a](https://doi.org/10.1039/c8me00099a).
  - 46 H.-M. Philp Chen, J. J. Ou and S. H. Chen, Glassy Liquid Crystals as Self-Organized Films for Robust Optoelectronic Devices, in *Nanoscience with Liquid Crystals*, ed. Q. Li, NanoScience and Technology, Springer International Publishing, 2014, pp. 179–208, DOI: [10.1007/978-3-319-04867-3\\_6](https://doi.org/10.1007/978-3-319-04867-3_6).
  - 47 T. Seshadri, H.-J. Haupt, U. Flörke and G. Henkel, Novel cholesteric glassy liquid crystals of monosubstituted ferrocenes: synthesis and selective reflection properties of a dimesogen, and crystal structure of a monomesogen, *Liq. Cryst.*, 2007, **34**(1), 33–47, DOI: [10.1080/02678290601033008](https://doi.org/10.1080/02678290601033008).
  - 48 M. Sorai and S. Seki, Glassy Liquid Crystal of the Nematic Phase of *N*-(*o*-Hydroxy-*p*-methoxybenzylidene)-*p*-butylaniline, *Bull. Chem. Soc. Jpn.*, 1971, **44**(10), 2887, DOI: [10.1246/bcsj.44.2887](https://doi.org/10.1246/bcsj.44.2887).
  - 49 K. Tsuji, M. Sorai and S. Seki, New Finding of Glassy Liquid Crystal – a Non-equilibrium State of Cholesteryl Hydrogen Phthalate, *Bull. Chem. Soc. Jpn.*, 1971, **44**(5), 1452, DOI: [10.1246/bcsj.44.1452](https://doi.org/10.1246/bcsj.44.1452).
  - 50 J. U. Wallace, A. Shestopalov, T. Kosci and S. H. Chen, Scalable Synthesis of Cholesteric Glassy Liquid Crystals, *Ind. Eng. Chem. Res.*, 2018, **57**(12), 4470–4473, DOI: [10.1021/acs.iecr.8b00667](https://doi.org/10.1021/acs.iecr.8b00667).
  - 51 A. Yildirim, P. Szymoniak, K. Sentker, M. Butschies, A. Bühlmeier, P. Huber, S. Laschat and A. Schönhals, Dynamics and ionic conductivity of ionic liquid crystals forming a hexagonal columnar mesophase, *Phys. Chem. Chem. Phys.*, 2018, **20**(8), 5626–5635, DOI: [10.1039/C7CP08186C](https://doi.org/10.1039/C7CP08186C).
  - 52 Y. Nozaki, K. Yamaguchi, K. Tomida, N. Taniguchi, H. Hara, Y. Takikawa, K. Sadakane, K. Nakamura, T. Konishi and K. Fukao, Phase Transition and Dynamics in Imidazolium-Based Ionic Liquid Crystals through a Metastable Highly Ordered Smectic Phase, *J. Phys. Chem. B*, 2016, **120**(23), 5291–5300, DOI: [10.1021/acs.jpcc.6b03804](https://doi.org/10.1021/acs.jpcc.6b03804).
  - 53 J. D. Holbrey and K. R. Seddon, The phase behaviour of 1-alkyl-3-methylimidazolium tetrafluoroborates; ionic liquids and ionic liquid crystals, *J. Chem. Soc., Dalton Trans.*, 1999, **13**, 2133–2140, DOI: [10.1039/A902818H](https://doi.org/10.1039/A902818H).
  - 54 Y. Biswas, P. Banerjee and T. K. Mandal, From Polymerizable Ionic Liquids to Poly(ionic liquid)s: Structure-Dependent Thermal, Crystalline, Conductivity, and Solution Thermoresponsive Behaviors, *Macromolecules*, 2019, **52**(3), 945–958, DOI: [10.1021/acs.macromol.8b02351](https://doi.org/10.1021/acs.macromol.8b02351).
  - 55 M. A. Kolmangadi, G. J. Smales, L. ZhuoQing, A. Yildirim, E. Wuckert, S. Eutonnat, F. Demel, P. Huber, S. Laschat and A. Schönhals, Side Chain Length-Dependent Dynamics and Conductivity in Self-Assembled Ion Channels, *J. Phys. Chem. C*, 2022, **126**(27), 10995–11006, DOI: [10.1021/acs.jpcc.2c03023](https://doi.org/10.1021/acs.jpcc.2c03023).
  - 56 J. Litterscheidt, J. S. Bandar, M. Ebert, R. Forschner, K. Bader, T. H. Lambert, W. Frey, A. Bühlmeier, M. Brändle, F. Schulz and S. Laschat, Self-Assembly of Aminocyclopropenium Salts: En Route to Deltic Ionic Liquid Crystals, *Angew. Chem., Int. Ed.*, 2020, **59**(26), 10557–10565, DOI: [10.1002/anie.202000824](https://doi.org/10.1002/anie.202000824).
  - 57 X. Li, D. W. Bruce and J. M. Shreeve, Dicationic imidazolium-based ionic liquids and ionic liquid crystals with variously positioned fluoro substituents, *J. Mater. Chem.*, 2009, **19**(43), 8232, DOI: [10.1039/B912873E](https://doi.org/10.1039/B912873E).
  - 58 S. Laschat, A. Baro, N. Steinke, F. Giesselmann, C. Hägele, G. Scalia, R. Judele, E. Kapatsina, S. Sauer, A. Schreivogel and M. Tosoni, Discotic liquid crystals: from tailor-made synthesis to plastic electronics, *Angew. Chem., Int. Ed.*, 2007, **46**(26), 4832–4887, DOI: [10.1002/anie.200604203](https://doi.org/10.1002/anie.200604203).
  - 59 T. Ichikawa, M. Yoshio, A. Hamasaki, S. Taguchi, F. Liu, X. Zeng, G. Ungar, H. Ohno and T. Kato, Induction of thermotropic bicontinuous cubic phases in liquid-crystalline ammonium and phosphonium salts, *J. Am. Chem. Soc.*, 2012, **134**(5), 2634–2643, DOI: [10.1021/ja209010m](https://doi.org/10.1021/ja209010m).
  - 60 T. Ichikawa, M. Yoshio, S. Taguchi, J. Kagimoto, H. Ohno and T. Kato, Co-organisation of ionic liquids with amphiphilic diethanolamines: construction of 3D continuous ionic nanochannels through the induction of liquid-crystalline bicontinuous cubic phases, *Chem. Sci.*, 2012, **3**(6), 2001, DOI: [10.1039/c2sc00981a](https://doi.org/10.1039/c2sc00981a).
  - 61 X. Gao, F. Lu, B. Dong, T. Zhou, Y. Liu and L. Zheng, Temperature-responsive proton-conductive liquid crystals formed by the self-assembly of zwitterionic ionic liquids, *RSC Adv.*, 2015, **5**(78), 63732–63737, DOI: [10.1039/c5ra10830f](https://doi.org/10.1039/c5ra10830f).
  - 62 B. Soberats, M. Yoshio, T. Ichikawa, H. Ohno and T. Kato, Zwitterionic liquid crystals as 1D and 3D lithium ion transport media, *J. Mater. Chem. A*, 2015, **3**(21), 11232–11238, DOI: [10.1039/c5ta00814j](https://doi.org/10.1039/c5ta00814j).
  - 63 T. Ichikawa, M. Yoshio, A. Hamasaki, J. Kagimoto, H. Ohno and T. Kato, 3D interconnected ionic nano-channels formed in polymer films: self-organization and polymerization of thermotropic bicontinuous cubic liquid crystals, *J. Am. Chem. Soc.*, 2011, **133**(7), 2163–2169, DOI: [10.1021/ja106707z](https://doi.org/10.1021/ja106707z).
  - 64 S. Yazaki, Y. Kamikawa, M. Yoshio, A. Hamasaki, T. Mukai, H. Ohno and T. Kato, Ionic Liquid Crystals: Self-assembly of Imidazolium Salts Containing an L-Glutamic Acid Moiety, *Chem. Lett.*, 2008, **37**(5), 538–539, DOI: [10.1246/cl.2008.538](https://doi.org/10.1246/cl.2008.538).
  - 65 M. Ichihara, A. Suzuki, K. Hatsusaka and K. Ohta, Discotic liquid crystals of transition metal complexes 37\*: a thermotropic cubic mesophase having Pnm symmetry exhibited by phthalocyanine-based derivatives, *Liq. Cryst.*, 2007, **34**(5), 555–567, DOI: [10.1080/02678290701284238](https://doi.org/10.1080/02678290701284238).
  - 66 S. Ujiie and A. Mori, Cubic Mesophase Formed by Thermotropic Liquid Crystalline Ionic Systems – Effects of Polymeric Counter Ion, *Mol. Cryst. Liq. Cryst.*, 2005, **437**(1), 25/[1269]–31/[1275], DOI: [10.1080/15421400590955479](https://doi.org/10.1080/15421400590955479).
  - 67 M. A. Alam, J. Motoyanagi, Y. Yamamoto, T. Fukushima, J. Kim, K. Kato, M. Takata, A. Saeki, S. Seki, S. Tagawa and



- T. Aida, "Bicontinuous cubic" liquid crystalline materials from discotic molecules: a special effect of paraffinic side chains with ionic liquid pendants, *J. Am. Chem. Soc.*, 2009, **131**(49), 17722–17723, DOI: [10.1021/ja905373d](#).
- 68 A. Mathis, M. Galin, J. C. Galin, B. Heinrich and C. G. Bazuin, Long alkyl chain dimethylammonioalkoxydicyanoethenolates as new zwitterionic thermotropic liquid crystals, *Liq. Cryst.*, 1999, **26**(7), 973–984, DOI: [10.1080/026782999204327](#).
- 69 X. Qiao, P. Sun, A. Wu, N. Sun, B. Dong and L. Zheng, Supramolecular Thermotropic Ionic Liquid Crystals Formed via Self-Assembled Zwitterionic Ionic Liquids, *Langmuir*, 2019, **35**(5), 1598–1605, DOI: [10.1021/acs.langmuir.8b03448](#).
- 70 R. Rondla, J. C. Y. Lin, C. T. Yang and I. J. B. Lin, Strong tendency of homeotropic alignment and anisotropic lithium ion conductivity of sulfonate functionalized zwitterionic imidazolium ionic liquid crystals, *Langmuir*, 2013, **29**(37), 11779–11785, DOI: [10.1021/la402336n](#).
- 71 B. Soberats, M. Yoshio, T. Ichikawa, S. Taguchi, H. Ohno and T. Kato, 3D Anhydrous proton-transporting nanochannels formed by self-assembly of liquid crystals composed of a sulfobetaine and a sulfonic acid, *J. Am. Chem. Soc.*, 2013, **135**(41), 15286–15289, DOI: [10.1021/ja407883b](#).
- 72 S. Liu, G. Yan, J. Wang, J. Zhou, L. Bie, Y. Jia and F. Meng, Self-assembly, phase behaviour and ion-conducting property of pyridinium-based ionic liquid-crystalline oligomers, *Liq. Cryst.*, 2021, **48**(2), 201–214, DOI: [10.1080/02678292.2020.1769753](#).
- 73 Y. V. Nelyubina, A. S. Shaplov, E. I. Lozinskaya, M. I. Buzin and Y. S. Vygodskii, A New Volume-Based Approach for Predicting Thermophysical Behavior of Ionic Liquids and Ionic Liquid Crystals, *J. Am. Chem. Soc.*, 2016, **138**(32), 10076–10079, DOI: [10.1021/jacs.6b05174](#).
- 74 W. Cao, B. Senthilkumar, V. Causin, V. P. Swamy, Y. Wang and G. Saielli, Influence of the ion size on the stability of the smectic phase of ionic liquid crystals, *Soft Matter*, 2020, **16**(2), 411–420, DOI: [10.1039/C9SM02115A](#).
- 75 N. De Vos, C. Maton and C. V. Stevens, Electrochemical Stability of Ionic Liquids: General Influences and Degradation Mechanisms, *ChemElectroChem*, 2014, **1**(8), 1258–1270, DOI: [10.1002/celec.201402086](#).
- 76 M. Hayyan, F. S. Mjalli, M. A. Hashim, I. M. AlNashef and T. X. Mei, Investigating the electrochemical windows of ionic liquids, *J. Ind. Eng. Chem.*, 2013, **19**(1), 106–112, DOI: [10.1016/j.jiec.2012.07.011](#).
- 77 S. Kazemiabnavi, Z. Zhang, K. Thornton and S. Banerjee, Electrochemical Stability Window of Imidazolium-Based Ionic Liquids as Electrolytes for Lithium Batteries, *J. Phys. Chem. B*, 2016, **120**(25), 5691–5702, DOI: [10.1021/acs.jpcc.6b03433](#).
- 78 U. A. Rana, R. Vijayaraghavan, M. Walther, J. Sun, A. A. J. Torriero, M. Forsyth and D. R. MacFarlane, Protic ionic liquids based on phosphonium cations: comparison with ammonium analogues, *Chem. Commun.*, 2011, 47(42), 11612–11614, DOI: [10.1039/c1cc14761g](#).
- 79 A. Gallastegui, F. Foglia, P. F. McMillan, N. Casado, A. Gueguen and D. Mecerreyes, Poly(diallylmethylammonium) proton conducting membranes with high ionic conductivity at intermediate temperatures, *Polymer*, 2023, **280**, 126064, DOI: [10.1016/j.polymer.2023.126064](#).
- 80 M. Martinez, Y. Molmeret, L. Cointeaux, C. Iojoiu, J.-C. Leprêtre, N. El Kissi, P. Judeinstein and J.-Y. Sanchez, Proton-conducting ionic liquid-based Proton Exchange Membrane Fuel Cell membranes: The key role of ionomer–ionic liquid interaction, *J. Power Sources*, 2010, **195**(18), 5829–5839, DOI: [10.1016/j.jpowsour.2010.01.036](#).
- 81 X. Lu, G. Burrell, F. Separovic and C. Zhao, Electrochemistry of room temperature protic ionic liquids: a critical assessment for use as electrolytes in electrochemical applications, *J. Phys. Chem. B*, 2012, **116**(30), 9160–9170, DOI: [10.1021/jp304735p](#).
- 82 T.-Y. Wu, S.-G. Su, Y.-C. Lin, H. P. Wang, M.-W. Lin, S.-T. Gung and I.-W. Sun, Electrochemical and physicochemical properties of cyclic amine-based Brønsted acidic ionic liquids, *Electrochim. Acta*, 2010, **56**(2), 853–862, DOI: [10.1016/j.electacta.2010.09.084](#).
- 83 C. Iojoiu, M. Martinez, M. Hanna, Y. Molmeret, L. Cointeaux, J.-C. Leprêtre, N. E. Kissi, J. Guindet, P. Judeinstein and J.-Y. Sanchez, PILs-based Nafion membranes: a route to high-temperature PEFMCs dedicated to electric and hybrid vehicles, *Polym. Adv. Technol.*, 2008, **19**(10), 1406–1414, DOI: [10.1002/pat.1219](#).
- 84 L. E. Shmukler, M. S. Gruzdev, N. O. Kudryakova, Y. A. Fadeeva, A. M. Kolker and L. P. Safonova, Thermal behavior and electrochemistry of protic ionic liquids based on triethylamine with different acids, *RSC Adv.*, 2016, **6**(111), 109664–109671, DOI: [10.1039/C6RA21360J](#).
- 85 J. C. Y. Lin, C.-J. Huang, Y.-T. Lee, K.-M. Lee and I. J. B. Lin, Carboxylic acid functionalized imidazolium salts: sequential formation of ionic, zwitterionic, acid-zwitterionic and lithium salt-zwitterionic liquid crystals, *J. Mater. Chem.*, 2011, **21**(22), 8110, DOI: [10.1039/c1jm10580a](#).
- 86 I. Bandrés, D. F. Montaña, I. Gascón, P. Cea and C. Lafuente, Study of the conductivity behavior of pyridinium-based ionic liquids, *Electrochim. Acta*, 2010, **55**(7), 2252–2257, DOI: [10.1016/j.electacta.2009.11.073](#).
- 87 A. Mariani, M. Bonomo, X. Gao, B. Centrella, A. Nucara, R. Buscaino, A. Barge, N. Barbero, L. Gontrani and S. Passerini, The unseen evidence of Reduced Ionicity: the elephant in (the) room temperature ionic liquids, *J. Mol. Liq.*, 2021, **324**, 115069, DOI: [10.1016/j.molliq.2020.115069](#).
- 88 S. Sen, S. E. Goodwin, P. V. Barbará, G. A. Rance, D. Wales, J. M. Cameron, V. Sans, M. Mamlouk, K. Scott and D. A. Walsh, Gel-Polymer Electrolytes Based on Poly(Ionic Liquid)/Ionic Liquid Networks, *ACS Appl. Polym. Mater.*, 2021, **3**(1), 200–208, DOI: [10.1021/acsapm.0c01042](#).
- 89 J. Vila, P. Ginés, J. M. Pico, C. Franjo, E. Jiménez, L. M. Varela and O. Cabeza, Temperature dependence of the electrical conductivity in EMIM-based ionic liquids, *Fluid Phase Equilib.*, 2006, **242**(2), 141–146, DOI: [10.1016/j.fluid.2006.01.022](#).
- 90 J. L. Ndeugueu, M. Ikeda and M. Aniya, Correlation between the temperature range of cooperativity and the fragility index in ion conducting polymers, *Solid State Ionics*, 2010, **181**(1–2), 16–19, DOI: [10.1016/j.ssi.2009.11.011](#).



- 91 S. Bulut, P. Eiden, W. Beichel, J. M. Slattery, T. F. Beyersdorff, T. J. S. Schubert and I. Krossing, Temperature dependence of the viscosity and conductivity of mildly functionalized and non-functionalized Tf<sub>2</sub>N(–) ionic liquids, *ChemPhysChem*, 2011, **12**(12), 2296–2310, DOI: [10.1002/cphc.201100214](https://doi.org/10.1002/cphc.201100214).
- 92 D. M. Correia, C. M. Costa, R. Sabater i Serra, J. Gómez Tejedor, L. Teruel Biosca, V. de Zea Bermudez, J. Esperança, P. M. Reis, A. Andrio Balado, J. M. Meseguer-Dueñas, S. Lanceros-Méndez and J. L. Gomez Ribelles, Molecular relaxation and ionic conductivity of ionic liquids confined in a poly(vinylidene fluoride) polymer matrix: influence of anion and cation type, *Polymer*, 2019, **171**, 58–69, DOI: [10.1016/j.polymer.2019.03.032](https://doi.org/10.1016/j.polymer.2019.03.032).
- 93 H. Pan, J. Luo, J. Zhao and M. Wubbenhorst, Multiple Phase Transitions and Temperature Dependent Ionic Conductivity of the Plastic Crystal Trioctylammonium Triflate Studied by Dielectric Spectroscopy and Calorimetry, *IEEE Trans. Dielectr. Electr. Insul.*, 2022, **29**(2), 526–533, DOI: [10.1109/TDEI.2022.3164064](https://doi.org/10.1109/TDEI.2022.3164064).
- 94 Q. Ruan, M. Yao, Y. Du, H. Dong, J. Liu, X. Yuan, W. Fang, G. Zhao and H. Zhang, Ionic liquid crystal electrolytes: fundamental, applications and prospects, *Nano Energy*, 2023, **106**, 108087, DOI: [10.1016/j.nanoen.2022.108087](https://doi.org/10.1016/j.nanoen.2022.108087).
- 95 X. Tang, X. Chang, B. Zhu, L. Cui, B. Jiang, F. Meng and G. Yan, Self-assembly, mesomorphic behavior, and ionic conductivity of polymerized ionic liquid crystals with a threshold switching characteristic, *Polym. Adv. Technol.*, 2022, **33**(12), 4317–4329, DOI: [10.1002/pat.5861](https://doi.org/10.1002/pat.5861).
- 96 S. Wang, X. Liu, A. Wang, Z. Wang, J. Chen, Q. Zeng, X. Wang and L. Zhang, An ionic liquid crystal-based solid polymer electrolyte with desirable ion-conducting channels for superior performance ambient-temperature lithium batteries, *Polym. Chem.*, 2018, **9**(37), 4674–4682, DOI: [10.1039/c8py00951a](https://doi.org/10.1039/c8py00951a).
- 97 J. Luo, O. Conrad and I. F. J. Vankelecom, Physicochemical properties of phosphonium-based and ammonium-based protic ionic liquids, *J. Mater. Chem.*, 2012, **22**(38), 20574, DOI: [10.1039/C2JM34359B](https://doi.org/10.1039/C2JM34359B).
- 98 I. Abdurrokhman, K. Elamin, O. Danyliv, M. Hasani, J. Swenson and A. Martinelli, Protic Ionic Liquids Based on the Alkyl-Imidazolium Cation: Effect of the Alkyl Chain Length on Structure and Dynamics, *J. Phys. Chem. B*, 2019, **123**(18), 4044–4054, DOI: [10.1021/acs.jpcc.9b01274](https://doi.org/10.1021/acs.jpcc.9b01274).

